Fracture parameters calibration and validation for the high strength steel based on the mesoscale failure index

Xin, Haohui; Correia, José A.F.O.; Veljkovic, Milan; Berto, Filippo

Important note
To cite this publication, please use the final published version (if applicable).
Please check the document version above.

Fracture parameters calibration and validation for the high strength steel based on the mesoscale failure index

Haohui Xin [a], José A.F.O. Correia [b],[*], Milan Veljkovic [c], Filippo Berto [d]

[a] Department of Civil Engineering, School of Human Settlements and Civil Engineering, Xi'an Jiaotong University, China
[b] CONSTRUCT, Faculty of Engineering, University of Porto, Portugal
[c] Faculty of Civil Engineering and Geosciences, Delft University of Technology, Netherlands
[d] Department of Mechanical and Industrial Engineering, Norwegian University of Science and Technology (NTNU), Norway

A B S T R A C T

Accurately obtaining the material parameters of the damage model is very important for the ductile fracture simulation of steel structures made of high strength steel (HSS). The combination of micromechanics with the uncoupled phenomenological fracture model can be used to obtain the material parameters of ductile fracture locus only from the uniaxial engineering stress-strain relationship. A micro failure index is generally used to link the material fracture under different multiaxial stress status. It is relatively difficult to describe the irregular micro-void evolution using the microvoid radius, and also difficult to tackle the micro void coalescence of the mesoscale using microvoid volume fraction. The mesoscale critical equivalent plastic strain (MCEPS) is proposed as the failure index at the unit cell level to calibrate the fracture locus of the uncoupled phenomenological model in this paper. The fracture locus of the HSS is calibrated by comparing the FE results with experimental data using the homogenized MCEPS and maximum MCEPS at the microvoid surface, respectively. The identified fracture locus is further validated against five stress status, including butterfly shear specimen, butterfly tension specimen, the tensile specimen with the symmetric round notch, tension specimen with a central hole in the middle, and Sandia fracture challenge specimens in 2014. The comparisons of predictions with the experimental results showed that the proposed MCEPS index can be used to obtain the material parameters of the ductile fracture locus.

1. Introduction

The high strength steel (HSS) can provide economical solutions for the highly loaded slender members applied in the long-span or high-rise structures [1–3]. The steel material generally has the option of either deformation or fracture when it reached its strength [4,5]. The HSS is usually manufactured very stronger by reducing the plastic deformation through reducing grain size, work hardening, etc. but has less deformation ability. In addition to the concerns of fatigue performance [6–9], the demands for the failure prediction of HSS structures or components are rising in the analysis and design because the HSS is always less ductile than the general mild structural steel. Material parameters identification of fracture models is the first step for the failure prediction of infrastructure made of HSS.

The failure of HSS is a progressive material deterioration due to the nucleation, growth, and coalescence of micro-voids [10]. The microvoids can be nucleated due to either matrix-particle de-cohesion or particle cracking. The microvoids nucleation is affected by the particle strength, size, and shape, as well as the hardening of the matrix material. The matrix-particle de-cohesion nucleation mechanism generally appeared for the soft matrix materials while the particle cracking nucleation mechanism generally occurred for the hard matrix materials. Besides, microvoids are easily appeared at large particles due to higher possibilities of defects and local stress fields generated by matrix plastic deformation. Noted that the nucleated voids are too small to have an obvious influence on the material macroscopic behaviors [11]. After the nucleation, the microvoids will become larger due to the plastic deformation. The micro void radius is proposed by Rice & Tracey in 1969 [12], and the void volume fraction is further adopted by Gurson in 1977 [13] to model the microvoid growth in terms of a perfect plastic matrix. The ductile fracture happened after the voids coalescence with the following two common modes [14], internal necking mode (Fig. 1 a-e),
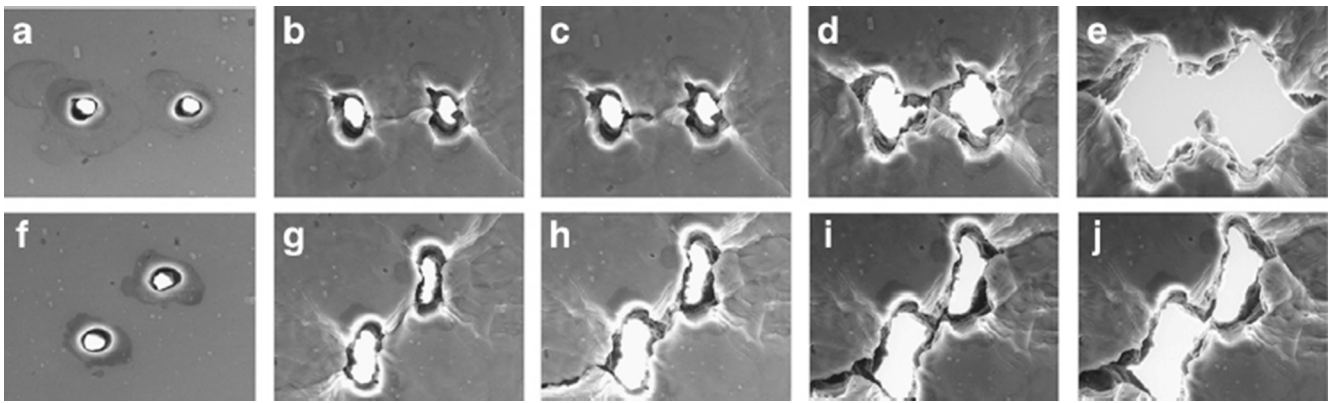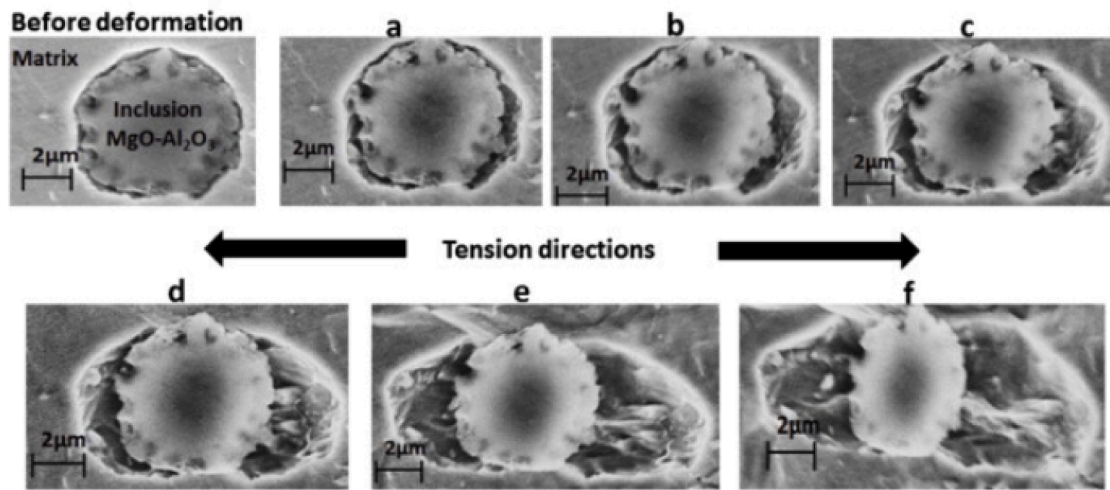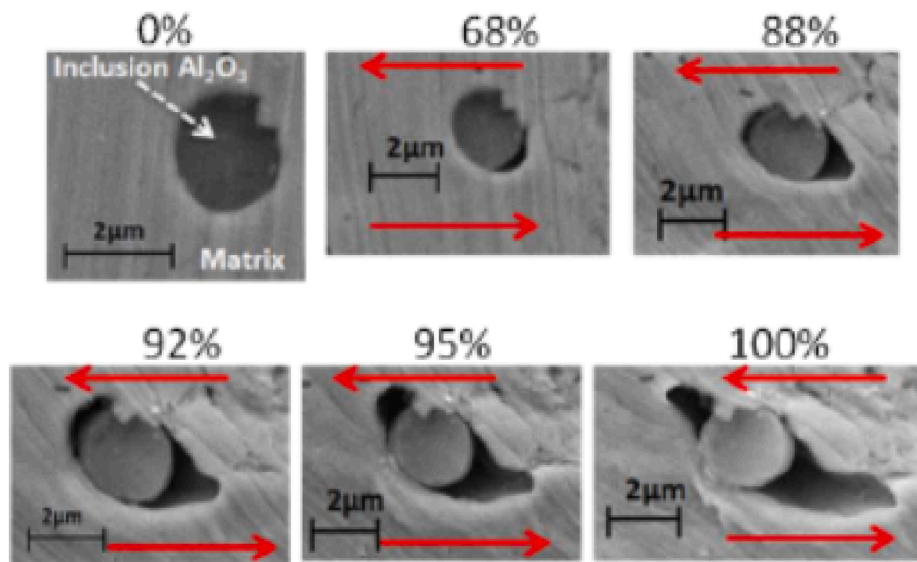
Fig. 1. Illustration of micro-voids coalescence [14].

(a) Exposed to tensile load

(b) Exposed to shear load

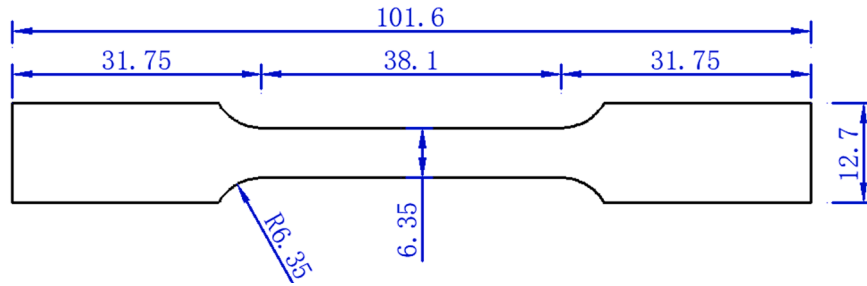**Fig. 2.** The micro-void evolution under tensile and shear loading [33].

Fig. 3. Tensile coupon specimens used to calibrate the stress-strain relationship with a thickness of 3.124 mm (Unit: mm).

shear localization mode (Fig. 1 f-j).

The fracture models of steels generally consist of physically-based [12,13,15–20] and phenomenological models [21–29]. The uncoupled phenomenological model [21–29], which assumed that the evolution of damage does not affect the effective stress-strain response of HSS before a fracture occurs, is generally adopted in engineering applications because the material parameters are more simple to be obtained compared with the physically-based model. The fracture locus of the uncoupled phenomenological damage model is highly related to the microvoid growth and coalescence process, which is dependent on the stress status and microstructures of the materials. Especially for low-stress triaxiality cases, large shape and relatively small volume changes are observed for the ductile fracture [14]. Hence, the critical equivalent plastic strain at the onset of fracture is the function of the stress triaxiality and the Lode (angle) parameter at the macro scale.

Although the parameters of the uncoupled phenomenological models are relatively easy to obtain, a series of experiments are needed to be conducted for each typical component to identify the parameters in the ductile fracture model. However, large civil structures are all different from each other and there is no serial production and the ductile performance of HSS from different steel grades, producers, manufacturing processes (cold-formed, hot rolled, etc.) varies a lot. It is also difficult to conduct all kinds of reliable experiments to generate different stress status through different initial specimen geometries or by applying different load combinations for typical parts in the civil engineering sector, such as welds, the heat-affected zone(HAZ), bolt, headed studs and fillet corners of cold-formed tube. The combination of mesoscale computational homogenization triggered by the physically-based model and uncoupled phenomenological model is promising to predict the
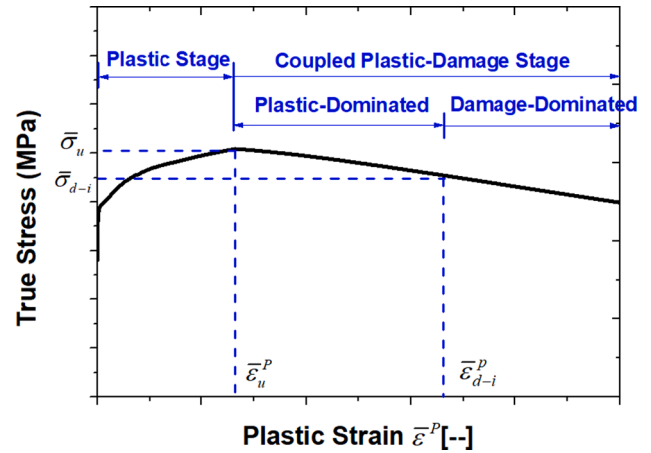
Fig. 4. Plastic and coupled plastic-damage stages [36] (Necking and damage effects are not considered for true stress).

Table 1
Calibrated parameters for coupled plastic-damage stage.

$\overline{\sigma}_u$	$\overline{\varepsilon}_u^p$	W	$\overline{\varepsilon}_{d-i}^p$	B
(MPa)	(–)	(–)	(–)	(–)
1198.10	0.0769	0.00	–	–
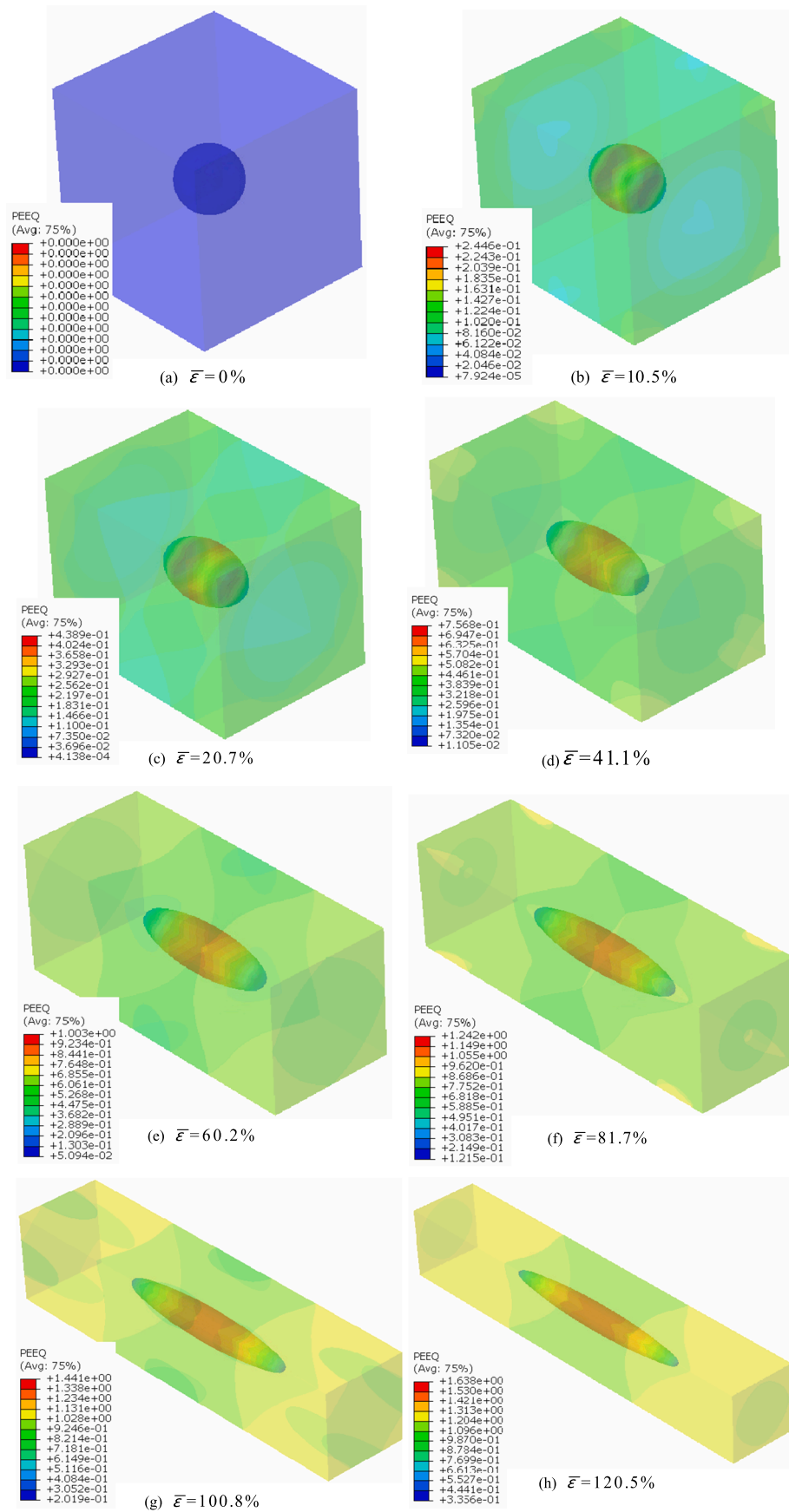
Fig. 5. Void Dilation of the unit cell exposed to uniaxial tension (Scale = 1.0).

(i) $\bar{\varepsilon} = 140.9\%$

(j) $\bar{\varepsilon} = 160.4\%$
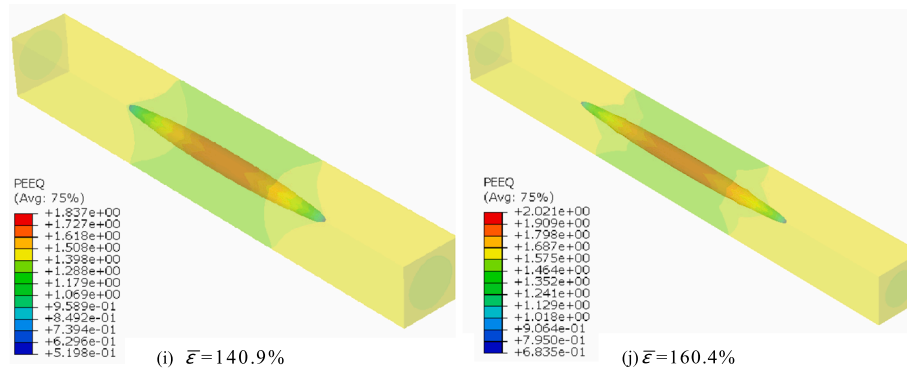
Fig. 5. (*continued*).

ductile fracture of HSS from only the uniaxial stress-strain relationship [30–32]. The mesoscale computational homogenization method could be used to identify the fracture strain at different stress status for the calibration of the parameters of the uncoupled phenomenological model.

A mesoscale failure index is generally used to predict the material failure under different multiaxial stress status, such as uniaxial tension, uniaxial compression, plane strain tension, plane strain compression, pure shear, combined tension-shear, and biaxial tension. The basic assumption is that the critical value of the mesoscale failure index is kept constant under multi-axial and non-proportional loading. As mentioned earlier, the micro void radius is proposed by Rice & Tracey in 1969 [12] as the mesoscale index. Base on the scanning electron microscope (SEM) in Fig. 2 [33], it is relatively difficult to describe the micro-void evolution by the micro void radius because the microvoid evolution is quite irregular. The void volume fraction is further adopted as the mesoscale failure index by Gurson in 1977 [13] to alleviate the micro-void shape effects. The rising questions will be how to model the micro void coalescence, as shown in Fig. 1. Hence, an attempt is made in this paper to use the other mesoscale failure index to describe the material fracture considering the "robustness" characteristics, namely (1) simple enough for the numerical implementation; and (2) convenient enough for parameters calibration.

In this paper, the mesoscale critical equivalent plastic strain (MCEPS) is proposed as the failure index at the unit cell level to calibrate the fracture locus of the uncoupled phenomenological model. The fracture locus of the HSS is calibrated by comparing the FE results with experimental data using the homogenized MCEPS and maximum MCEPS at the microvoid surface, respectively. The identified fracture locus is further validated against five stress status, including butterfly shear specimen, butterfly tension specimen, the tensile specimen with the symmetric round notch, tension specimen with a central hole in the middle, and Sandia fracture challenge specimens in 2014.

2. Material parameters identification

To predict the ductile fracture of high strength steels, this paper divided the identification process into two stages:①Identify the relationship between equivalent plastic strain and uniaxial true stress for the isotropic J2 plasticity model;②Identify parameters of fracture strain under multiaxial stress states. Noted that the evolution of damage does not affect the uniaxial true stress-strain response of HSS before a fracture occurs.

2.1. Plastic flow stress

All the test specimens [34] were cut from a high strength steel plate with a measured thickness of 3.124 mm. Four specimens, two identical specimens as one group in terms of orientation, were tested to obtain the engineering stress-strain curves. The geometry of tensile coupon specimens is shown in Fig. 3 based on the ASTM E8 standard [35].

As shown in Fig. 4, the division of the whole uniaxial stress-strain relationship is into three stages: elastic stage, plastic stage, and coupled plastic-damage stage [36]. The coupled plastic-damage stage is further decomposed into the plastic-dominated zone and the damage-dominated zone. The elastic stage is controlled by the elastic strain and elastic modulus. The plastic and coupled plastic-damage stages are presented in Fig. 4.

The material is exposed to the plastic stage when the equivalent plastic stage is $0 \leqslant \bar{\varepsilon}^p \leqslant \bar{\varepsilon}_u^p$. $\bar{\varepsilon}_u^p$ is the corresponding plastic strain when the true stress without considering necking and damage effects reached the peak. In the plastic stage, the uniaxial plastic strain and true stress are

(a) $\overline{\varepsilon}=0\%$

(b) $\overline{\varepsilon}=4.9\%$

(c) $\overline{\varepsilon}=10.4\%$

(d) $\overline{\varepsilon}=20.6\%$

(e) $\overline{\varepsilon}=40.0\%$

(f) $\overline{\varepsilon}=60.1\%$

(g) $\overline{\varepsilon}=79.6\%$

(h) $\overline{\varepsilon}=99.7\%$
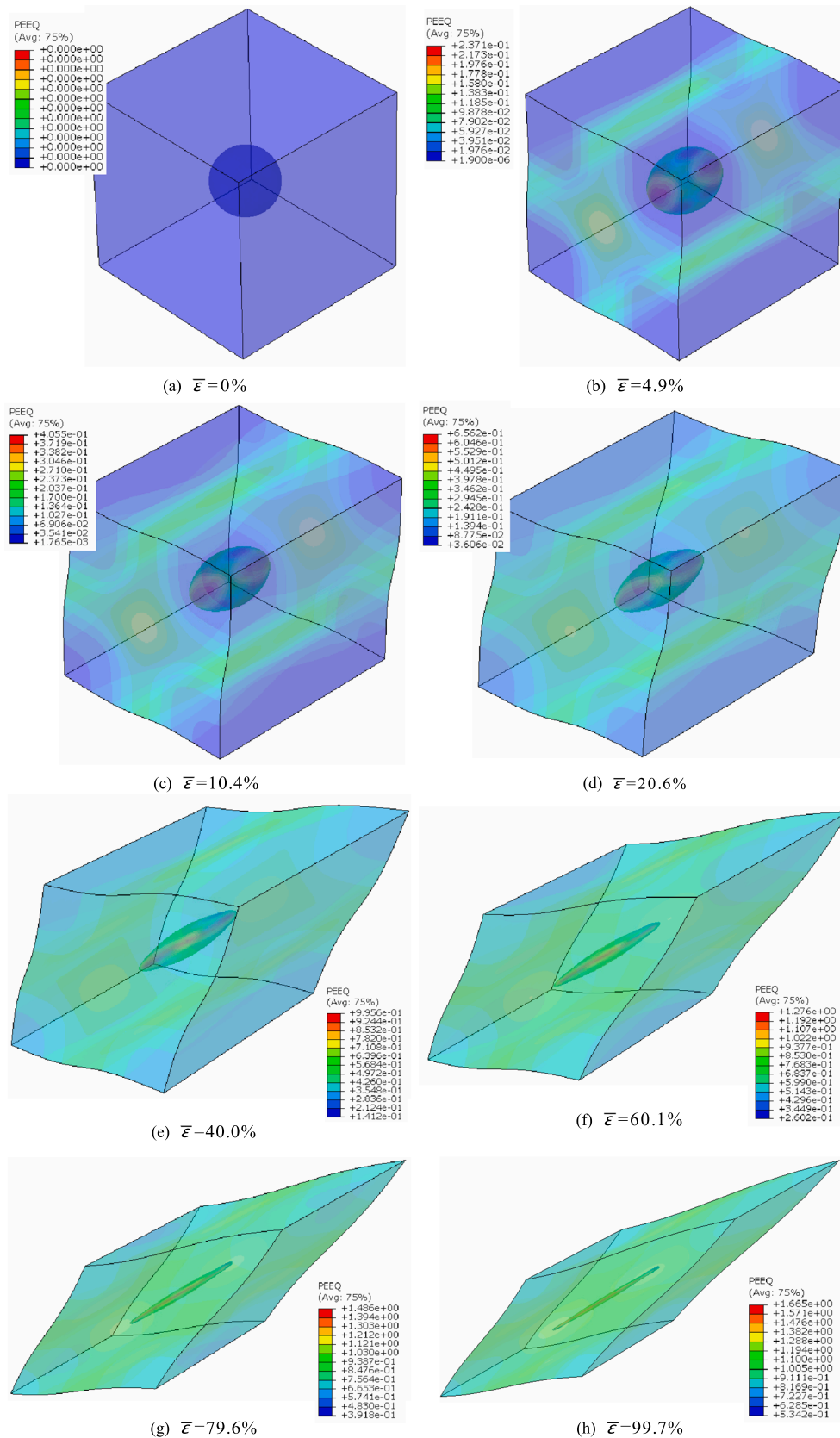
Fig. 6. Shear-dominated void deformation of the unit cell exposed to pure shear (Scale = 1.0).

(i) $\overline{\varepsilon} = 119.9\%$
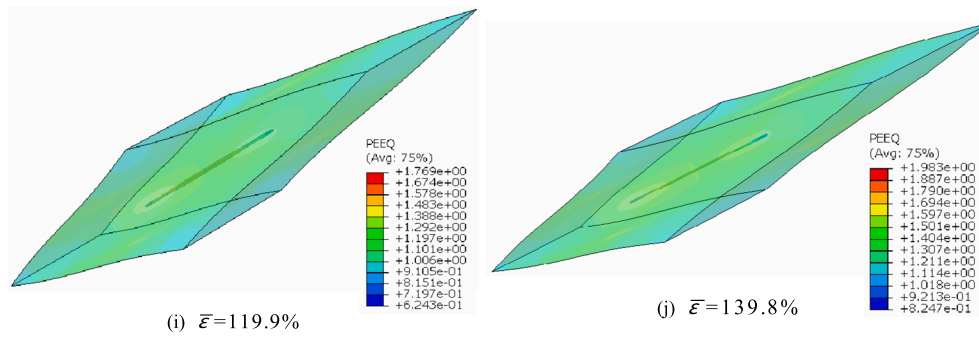

(j) $\overline{\varepsilon} = 139.8\%$

Fig. 6. (*continued*).

simply obtained through the engineering strain-engineering stress relationship. When $\overline{\varepsilon}_u^p > \overline{\varepsilon}^p$, the coupled plastic-damage stage reached. The point of maximum true stress is the onset of the necking. When $\overline{\varepsilon}_u^p < \overline{\varepsilon}^p \leqslant \overline{\varepsilon}_{d-i}^p$, the plasticity is dominated in the coupled plastic-damage stage. The weighted function [37], as expressed in Eq. (1), is used to predict the true stress after necking.

$$\overline{\sigma}^{neck} = \overline{\sigma}_u \left[W \left(1 \; + \; \overline{\varepsilon}^p \; - \; \overline{\varepsilon}_u^p \right) + (1 - W) \left(\frac{\left(\overline{\varepsilon}^p \right)^{\overline{\varepsilon}_u^p}}{\left(\overline{\varepsilon}_u^p \right)^{\overline{\varepsilon}_u^p}} \right) \right] \quad (1)$$

Where: W is a weight constant, $0 \leqslant W \leqslant 1$.

When $\overline{\varepsilon}^p > \overline{\varepsilon}_{d-i}^p$, the damage is dominated in the coupled plastic-damage stage, see Fig. 4. The true stress in the damage-dominated zone could be obtained through Eq. (2). The damage evolution law, expressed in Eq. (3), is adopted to determine the dependence of the damage scalar d on the equivalent plastic strain $\overline{\varepsilon}^p$. The measured engineering stress-engineering strain relationship is considered as a target, the parameter B is varied in the finite element model until the calculated engineering curves agree well with the experimental results [36]. The calibrated parameters for the coupled plastic-damage stage are summarized in Table 1.

$$\overline{\sigma} = (1 - d)\overline{\sigma}^{neck} \quad (2)$$

$$d = \begin{cases} 0 & \overline{\varepsilon}^p < \overline{\varepsilon}_{d-i}^p \\ 1 - exp \left[- B \left(\overline{\varepsilon}^p - \overline{\varepsilon}_{d-i}^p \right) \right] & \overline{\varepsilon}^p \geqslant \overline{\varepsilon}_{d-i}^p \end{cases} \quad (3)$$

2.2. Computational homogenization

The cubic with a void in the middle is assumed to be the unit cell. The initial void volume fraction is assumed to 0.5%. The link between micro-scale and macro-scale behavior could be established based on Hill-Mandel computational homogenization method. The macro-scale Cauchy stress σ_{ij} is obtained by averaging the micro-scale Cauchy stress, $\widetilde{\sigma}_{ij}$, in the unit cell domain, expressed as below [38]:

$$\sigma_{ij} = \frac{1}{|\Theta|} \int_\Theta \widetilde{\sigma}_{ij} d\Theta \quad (4)$$

where: σ_{ij} is the macro-scale Cauchy stress, $\widetilde{\sigma}_{ij}$ is the micro-scale Cauchy stress, Θ is the domain of the unit cell. Because the initial void volume fraction is quite small, the uniaxial true stress-strain curves of HSS is used as the matrix in this paper. The so-called "mixed boundary conditions" was implemented through the constraint equations in the ABAQUS software [39] by the following equations:

$$\int_{\partial\Theta_Y} \left(u_i^f(x,y) - \varepsilon_{ik}^c y_k \right) N_j^\Theta d\gamma_Y = 0 \quad (5)$$

$$\left| u_i^f(x,y) - \varepsilon_{ik}^c y_k \right| N_j^\Theta \leqslant Tol \quad (6)$$

where: N_j^Θ is the unit normal to the unit cell boundary $\partial\Theta_y$, x is the coordinate system at the macro scale, y is the coordinate system at the micro-scale. ε_{ik}^c is the strain tensor at the macro scale, u_i^f is the displacement vector at the micro scale.

The three-dimensional micro-void deformation of the unit cell under uniaxial tension (UT) is shown in Fig. 5. In terms of the unit cell exposed to uniaxial tensile, the micro-void is expanded along the loading
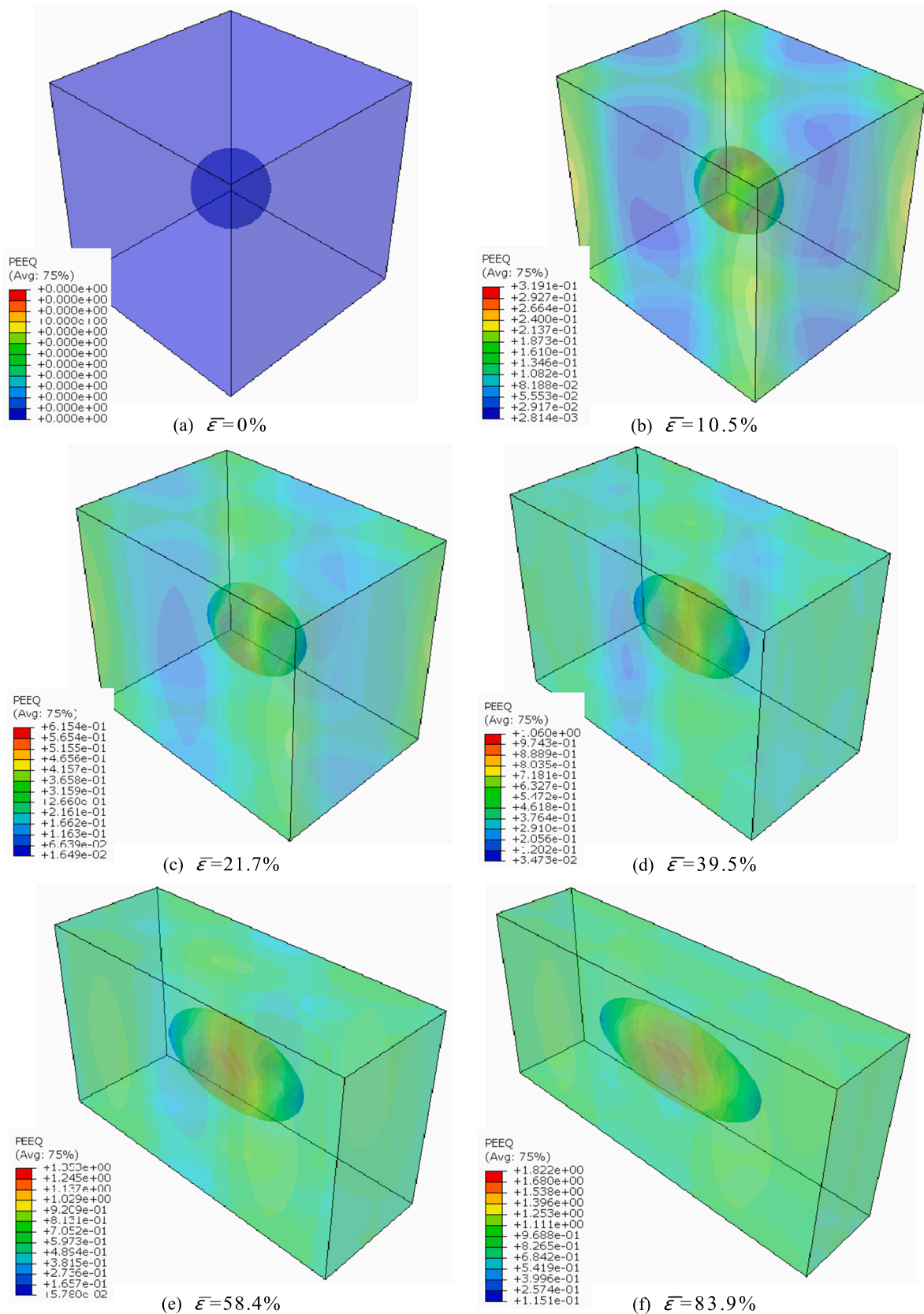
Fig. 7. Void deformation of the unit cell exposed to plain strain tension (Scale = 1.0).
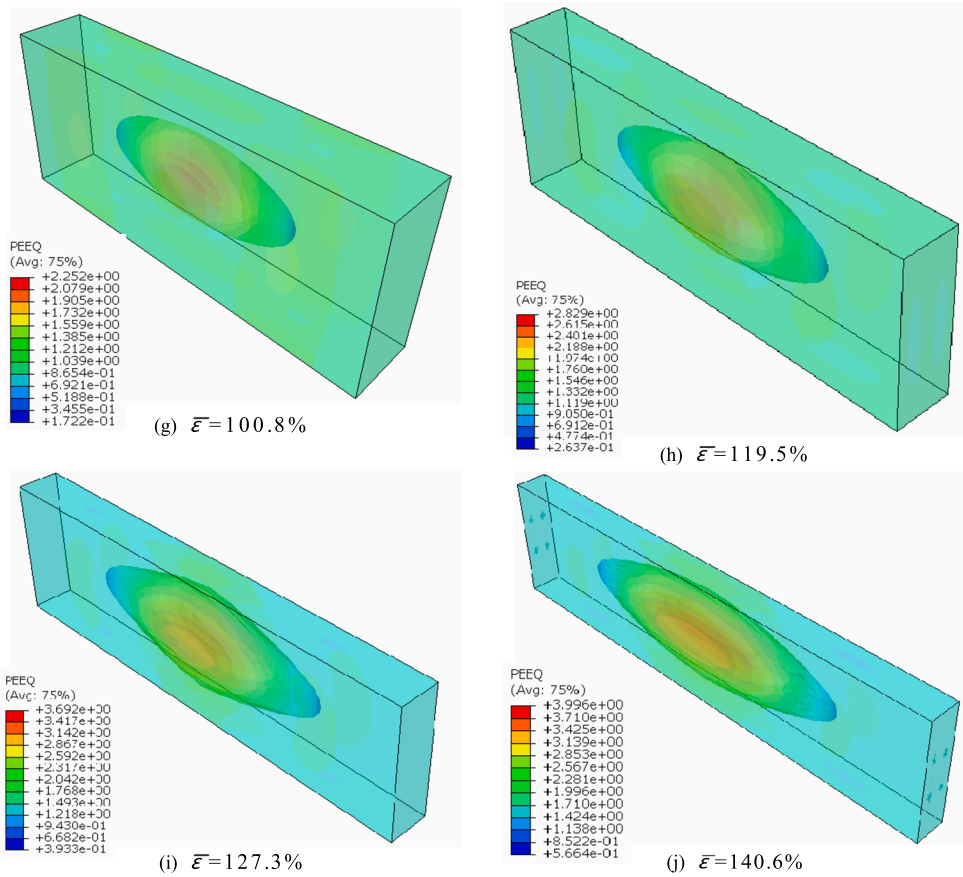
(g) $\bar{\varepsilon} = 100.8\%$

(h) $\bar{\varepsilon} = 119.5\%$

(i) $\bar{\varepsilon} = 127.3\%$

(j) $\bar{\varepsilon} = 140.6\%$

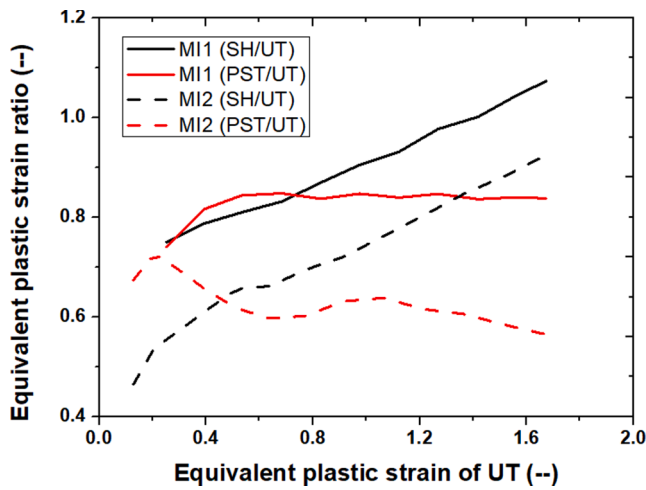**Fig. 7.** (*continued*).

Fig.8. Equivalent plastic strain ratio evolution with stretching exposed to pure tension.
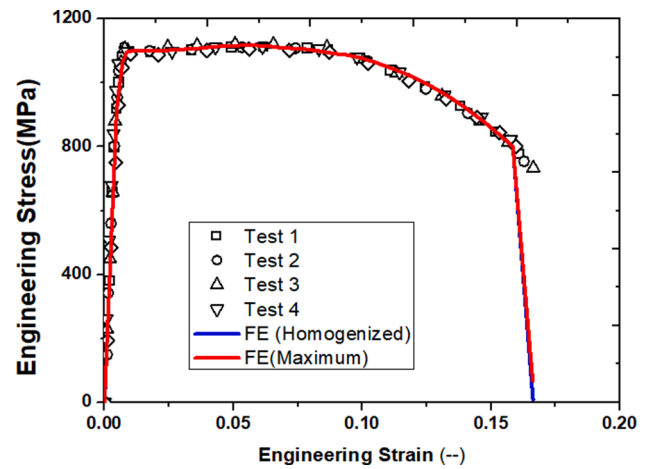

Fig. 9. Calibration of fracture strain exposed to uniaxial loading using different mesoscale failure index.

Table 2
Fitted coefficients of the polynomial expression.

Item		ξ_1	ξ_2	ξ_3	ξ_4	ξ_5	ξ_6	ξ_7
MI_1	$r_{SH/UT}$	0.4594	2.3230	−6.8023	10.4730	−8.3510	3.3340	−0.5266
	$r_{PST/UT}$	0.3185	2.8083	−5.7812	5.7804	−2.8630	0.6040	−0.0251
MI_2	$r_{SH/UT}$	0.3235	1.3663	−2.0732	1.1213	0.5242	−0.6948	0.1763
	$r_{PST/UT}$	0.3518	4.4037	−18.4010	33.0220	−29.1780	12.5330	−2.0958
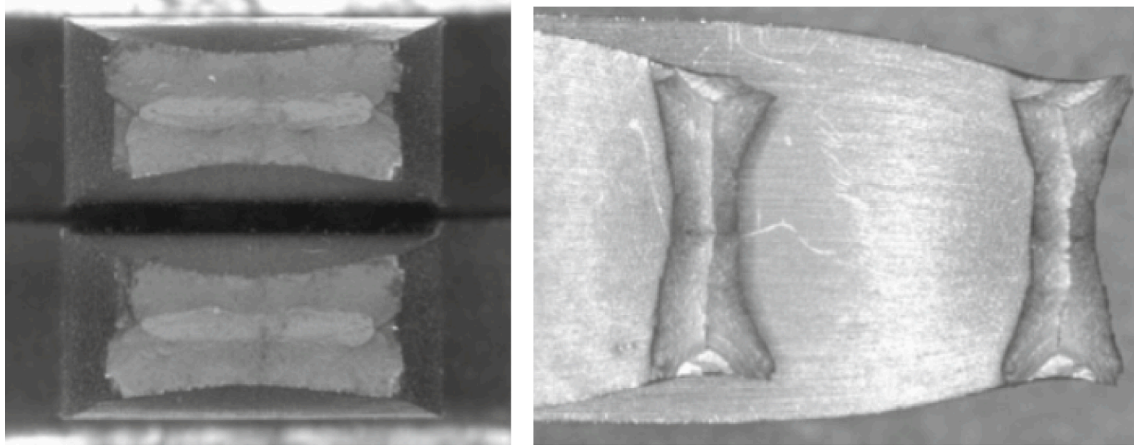
(a) Experimental failure mode[34]
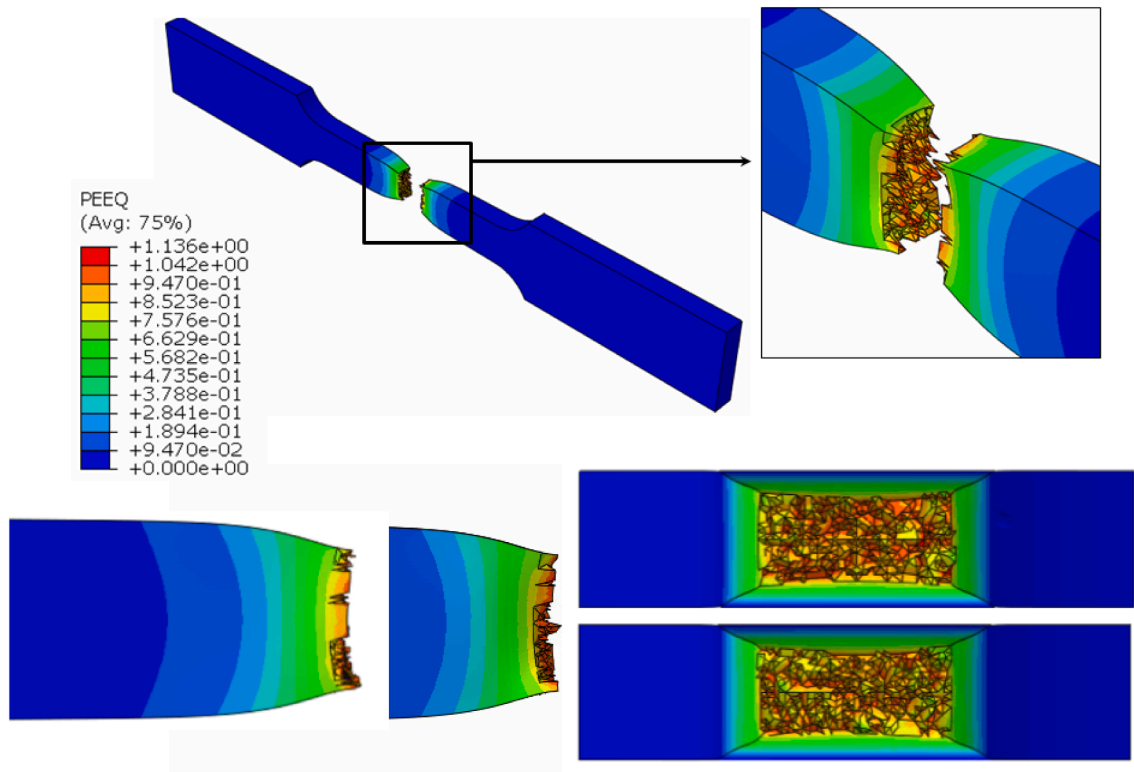
(b) MI$_1$ as the mesoscale indicator

Fig. 10. Failure mode comparisons between FE simulation and test results.

(c) MI$_2$ as the mesoscale indicator
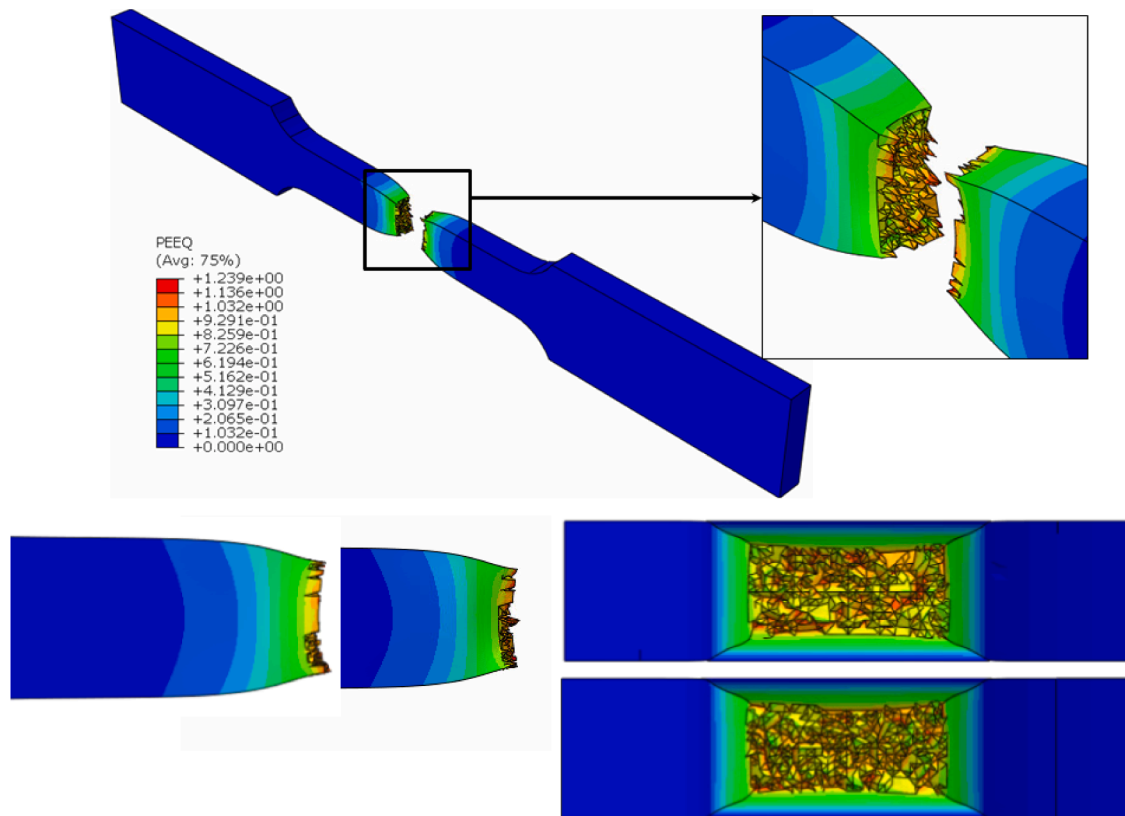
Fig. 10. (*continued*).

direction while is shrinkage vertical to the loading direction with the tensile loading increasing. The initial sphere is gradually changed to an ellipsoid when the macro equivalent strain increased to 70.6%. The maximum mesoscale equivalent plastic strain (MMEPS) around the microvoid surface is gradually increased to 202.1% when $\bar{\varepsilon} = 160.4\%$. The ratio between MMEPS and $\bar{\varepsilon}$ is 2.33 when $\bar{\varepsilon} = 10.5\%$, and is decreased to 1.26 when $\bar{\varepsilon} = 160.4\%$.

Fig. 6 illustrated the three-dimensional micro-void deformation of the unit cell exposed to pure shear. In terms of the unit cell exposed to shear loading, the micro-void is expanded along 45°Counterclockwise while is shrinkage along −45°Counterclockwise. The MMEPS is gradually increased to 198.3% when $\bar{\varepsilon} = 139.8\%$. The ratio between MMEPS and $\bar{\varepsilon}$ is 4.84 when $\bar{\varepsilon} = 4.9\%$, and is decreased to 1.42 when $\bar{\varepsilon} = 139.8\%$.

Noted that it is not straightforward using strain-controlled loading to generate the plane strain tension (PST) status. A parametric study is

carried out to generate the PST stress status by changing the ratio between macro strain ε_{11} and macro strain ε_{22}. Noted that the other type of macro strain is assumed to be free during the parametric analysis. The results showed that the macro stress status is close to PST status when the $\varepsilon_{22} = 0.01\varepsilon_{11}$. The three-dimensional micro-void deformation of the unit cell exposed to PST loading is shown in Fig. 7. The MMEPS is gradually increased to 399.6% when $\bar{\varepsilon} = 140.6\%$. The ratio between MMEPS and $\bar{\varepsilon}$ is 3.04 when $\bar{\varepsilon} = 10.5\%$, and is decreased to 2.84 when $\bar{\varepsilon} = 140.6\%$. The micro-void is also shrinkage along the vertical direction because of the Poisson's ratio effects although a small vertical macro strain ε_{22} is applied.

The authors postulated that the ductile fracture of the macro scale is due to the concentration in the microscale. We define the mesoscale critical equivalent plastic strain (MCEPS) on the microvoid surface Γ_v as the mesoscale indicator to illustrate the material failure. It is assumed that the MCEPS of the unit cell is kept constant when the material is
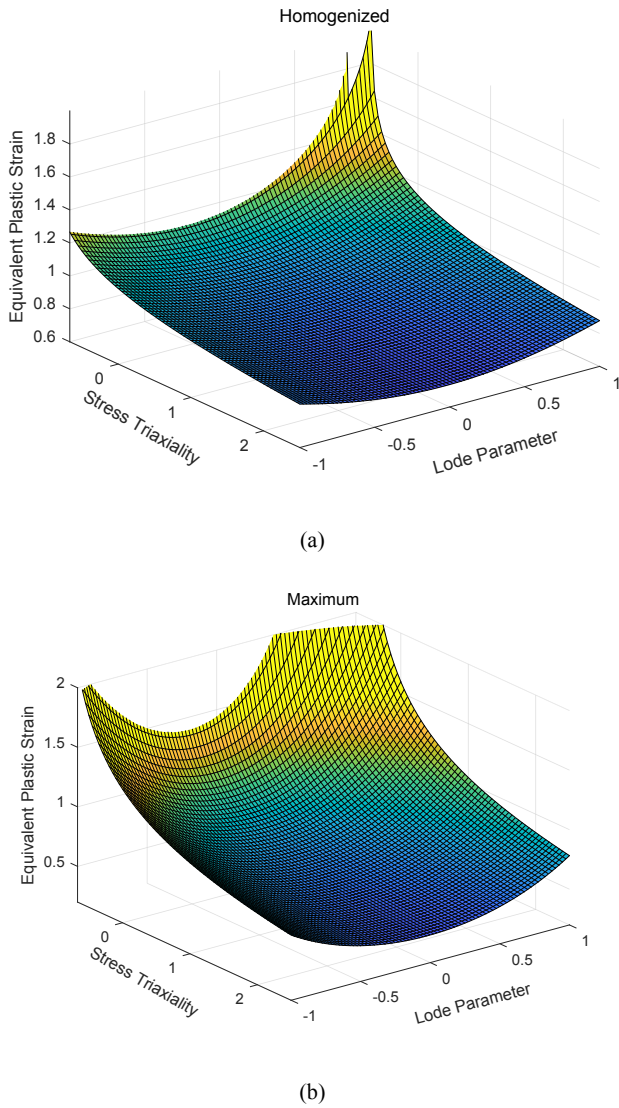
(a)

(b)

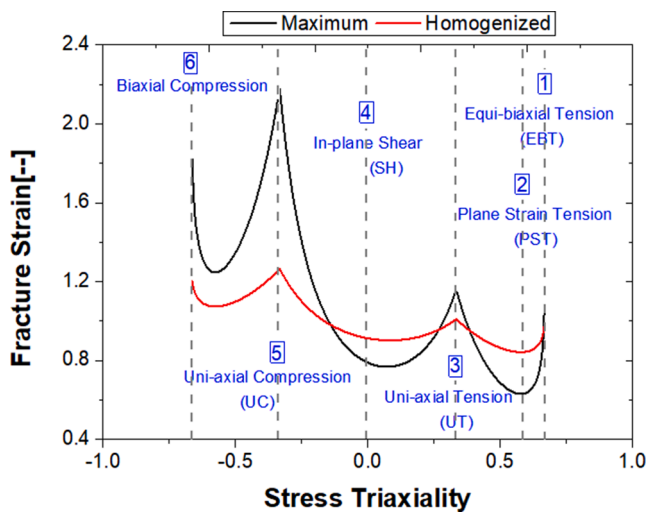**Fig. 11.** Fracture locus as a function of the stress triaxiality and Lode parameter.

Fig. 12. Fracture strain vs. stress triaxiality exposed to plane stress statues.

exposed to multiaxial loading. Two mesoscale indicators (MIs) are proposed, as expressed in Eqs. (7) and (8), to predict the failure. Homogenized MCEPS MI_1 defines the homogenized equivalent strain at the microvoid surface to be the mesoscale failure index, while maximum MCEPS MI_2 defines the maximum equivalent strain at the microvoid surface to be the mesoscale failure index.

$$MI_1 = \frac{1}{|\Gamma_v|} \int_{\Gamma_v} \overline{\varepsilon}^p d\Gamma \qquad (7)$$

$$MI_2 = \max(\Gamma_v \overline{\varepsilon}^p) \qquad (8)$$

The equivalent plastic strain with the same *MI* value is extracted for the unit cell loaded by the uniaxial tension(*UT*), shear(*SH*), and plane strain tension(*PST*) respectively, presented in Fig. 8. Because the fracture strain exposed to uniaxial tension(*UT*) is not determined, the fracture strain ratio, *SH* to *UT,* and also *PST* to *UT*, is plotted against the evolution of fracture strain exposed to uniaxial tension. And the relationship between strain ratio and fracture strain exposed to uniaxial strain is fitted by seven-term polynomial expression. The fitted coefficients are summarized in Table 2.

$$r_\chi = \sum_{i=1}^{7} \xi_i \left(\overline{\varepsilon}_{UT}^p \right)^{i-1} \quad \chi = "SH/UT", "PST/UT" \qquad (9)$$

where: $r_{SH/UT}$ is the fracture strain ratio between pure shear (SH) loading and uniaxial tensile loading (UT); $r_{PST/UT}$ is the fracture strain ratio between plane strain tensile (PST) loading and uniaxial tensile (UT) loading; ξ_i is the coefficient of polynomial expression; $\overline{\varepsilon}_{UT}^p$ is the fracture strain exposed to uniaxial tension.

2.3. Fracture locus identification

The micro-mechanism-motivated model proposed by Lou et al. [28,29], as expressed in Eq. (10), is used to identify the fracture locus.

$$\overline{\varepsilon}_f^p = C_3 \left(\frac{\sqrt{\overline{L}^2 + 3}}{2} \right)^{C_1} \left[\frac{1}{1 + C} \left(\overline{\eta} + \frac{3 - \overline{L}}{3\sqrt{\overline{L}^2 + 3}} + C \right) \right]^{-C_2} \qquad (10)$$

where: $\overline{\eta}$ and $\overline{L}$ is the stress triaxiality and the Lode parameters averaged over the loading history to consider the non-proportional loading effects, as expressed in Eqs. (11) and (12). C is the cut-off value and is assumed to be 1/3 in this paper.

$$\overline{\eta} = \frac{1}{\overline{\varepsilon}_f^p} \int_0^{\overline{\varepsilon}_f^p} \eta d\overline{\varepsilon}^p \qquad (11)$$

$$\overline{L} = \frac{1}{\overline{\varepsilon}_f^p} \int_0^{\overline{\varepsilon}_f^p} L d\overline{\varepsilon}^p \qquad (12)$$

The stress triaxiality η and the Lode parameter L is given by:

$$\eta = \frac{\sigma_m}{\overline{\sigma}} = \frac{\sigma_1 + \sigma_2 + \sigma_3}{3\overline{\sigma}} \qquad (13)$$

$$L = \frac{2\sigma_2 - \sigma_1 - \sigma_3}{\sigma_1 - \sigma_3} \qquad (14)$$

where: $\sigma_i (i = 1, 2, 3)$ is the principal stress.

For uniaxial tensile (UT), $\eta = \frac{1}{3}$ and $L = -1$. For pure shear (SH), $\eta = 0$ and $L = 0$. For plane strain tension(PST), $\eta = \frac{1}{\sqrt{3}}$ and $L = 0$. Hence, the parameters of Eq. (10) could be calculated using equivalent fracture plastic strain exposed to uniaxial tensile $\overline{\varepsilon}_{UT}^p$, exposed to shear $\overline{\varepsilon}_{SH}^p$, and exposed to plane strain tension $\overline{\varepsilon}_{PST}^p$ as follows:

Table 3
Parameters of damage model and fracture strain at different stress status.

Item	C_1	C_2	C_3	$\bar{\varepsilon}^p_{EBT}$	$\bar{\varepsilon}^p_{PST}$	$\bar{\varepsilon}^p_{UT}$	$\bar{\varepsilon}^p_{SH}$	$\bar{\varepsilon}^p_{UC}$	$\bar{\varepsilon}^p_{EBC}$
MI_1	1.141	0.163	1.010	0.98	0.84	1.01	0.91	1.26	1.20
MI_2	3.894	0.456	1.160	1.05	0.63	1.16	0.79	2.18	1.82

(a) Geometry (Unit: mm) [40]

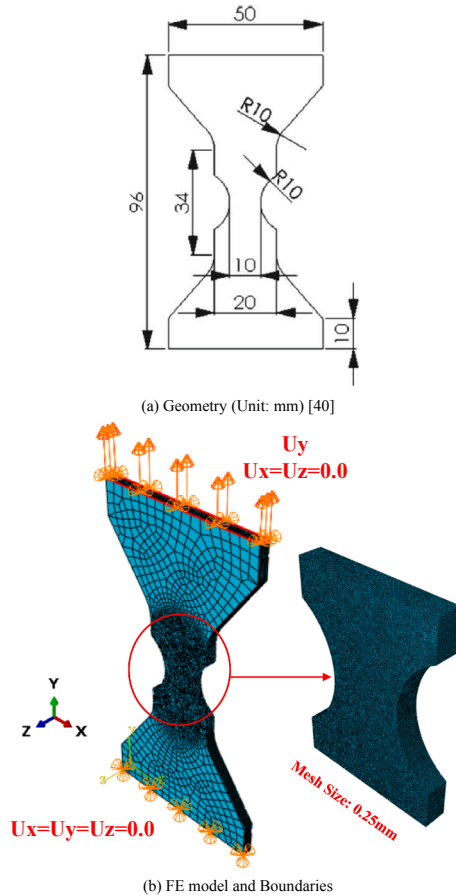
(b) FE model and Boundaries

Fig. 13. Specimens with the symmetric round notch (RN) with a thickness of 3.124 mm.
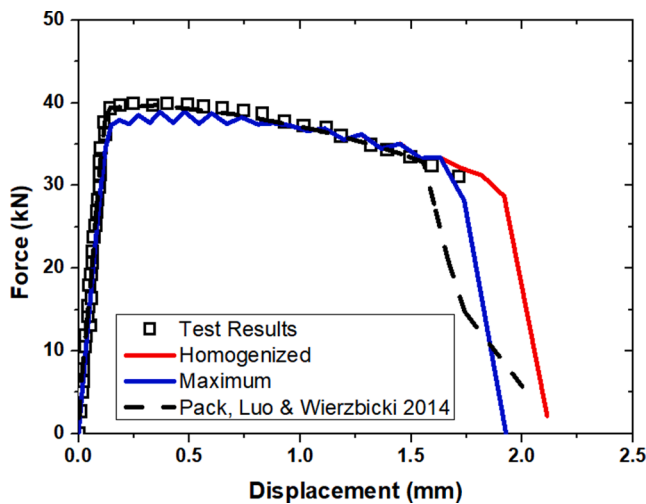

Fig. 14. Comparisons of force-displacement of RN specimen between experimental observations and finite element simulation.

$$C_1 = log_{\left(\frac{2}{\sqrt{3}}\right)}\left[\frac{\bar{\varepsilon}^p_{UT}}{\bar{\varepsilon}^p_{SH}}\frac{(1/\sqrt{3}+C)}{(2/\sqrt{3}+C)}\right]^{-C_2} \tag{15}$$

$$C_2 = log_{\left(\frac{1/\sqrt{3}+C}{2/\sqrt{3}+C}\right)}\left(\frac{\bar{\varepsilon}^p_{PST}}{\bar{\varepsilon}^p_{SH}}\right) \tag{16}$$

$$C_3 = \bar{\varepsilon}^p_{UT} \tag{17}$$

The equivalent fracture plastic strain relationship, $r_{SH/UT}$, which is the ratio between shear $\bar{\varepsilon}^p_{SH}$ and uniaxial tensile $\bar{\varepsilon}^p_{UT}$, and, $r_{PST/UT}$, that is the ratio between plane strain tension $\bar{\varepsilon}^p_{PST}$ and uniaxial tensile $\bar{\varepsilon}^p_{UT}$, is already obtained based on the proposed MCEPS. The fracture strain exposed to uniaxial tensile could be determined through the calibration by comparing the FE results against the experimental results with the ratio $r_{SH/UT}$ and $r_{PST/UT}$ obtained by the different mesoscale indicators. As shown in Fig. 9, the fracture strain exposed to uniaxial tension is determined to be 1.01 based on the MI_1 mesoscale failure index and 1.16 based on the MI_2 mesoscale failure index respectively, when the simulated uniform elongation reached the average value of four coupon tests. The failure mode comparisons between FE simulation and experimental observations are shown in Fig. 10. A good agreement is observed.

The fracture locus is a function of the stress triaxiality and the Lode parameter, illustrated in Fig. 11. For plane stress conditions, the Lode parameter is a function of the stress triaxiality. The fracture locus exposed to plane stress status with a function of the stress triaxiality is shown in Fig. 12. The results showed that the fracture strain calibrated based on the MI_1 failure index is larger than it using the MI_2 failure index when $-0.14 \leqslant \eta \leqslant 0.27$ and $0.38 \leqslant \eta \leqslant 0.66$ while the fracture strain calibrated based on the MI_1 failure index is smaller than it using the MI_2 failure index when $\eta > 0.66$, $\eta < -0.14$ and $0.27 < \eta < 0.38$. The material parameters of the damage model and the fracture strains fracture exposed to uniaxial tension(UT), plane strain tension(PST), equal biaxial tension (EBT), in-plane shear(SH), uniaxial compression(UC), and equal biaxial compression (EBC) are listed in Table 3.

3. Validation of fracture locus

To validate the identified fracture locus, the ductile fractures of butterfly shear (BS)specimen, butterfly tension (BT)specimen, the tensile specimen with the symmetric round notch(RN), tension specimen with a central hole in the middle(CN) are simulated. The results of FE simulation results are compared with experimental results[40], and also FE prediction using the calibrated MMC model based on the test series reported in this section [40]. Noted that the key areas of all specimens were simulated by solid element C3D10 with a fixed mesh size of 0.25 mm to avoid the mesh size effects on the FE results.

3.1. Specimens with symmetric notches

The geometry, mesh, and boundary conditions of RN specimens are illustrated in Fig. 13. The force–displacement comparisons of RN specimens between experimental observations and finite element simulation are shown in Fig. 14. The predicted fracture displacement from maximum MCEPS and literature [40] is smaller than test results, and it from homogenized MCEPS is larger than the test results.

The crack propagation and the evolution of stress triaxiality and the
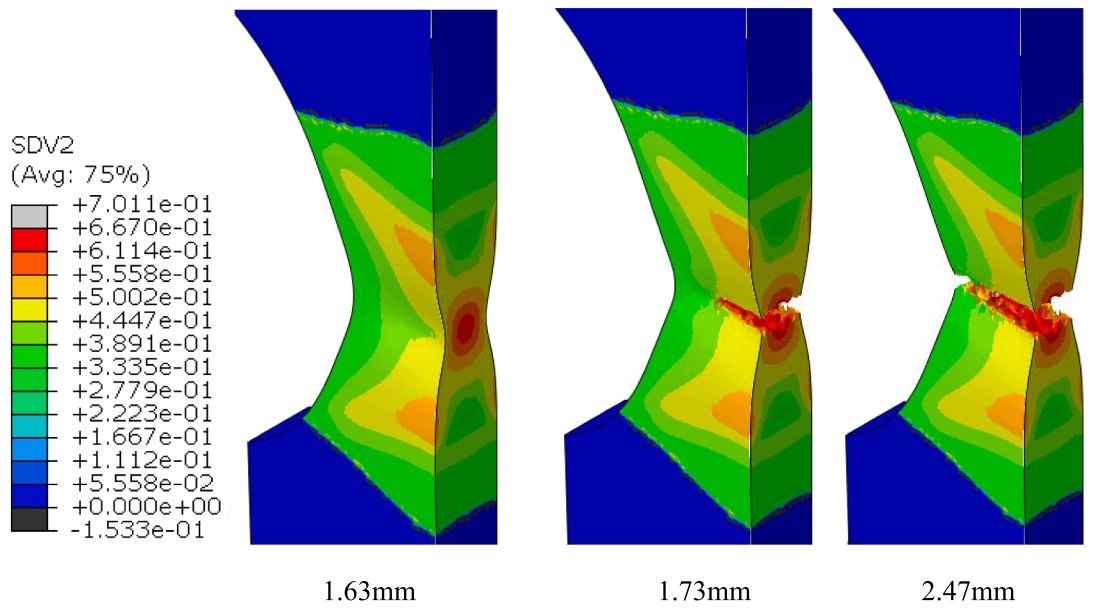
(a) $\bar{\eta}$
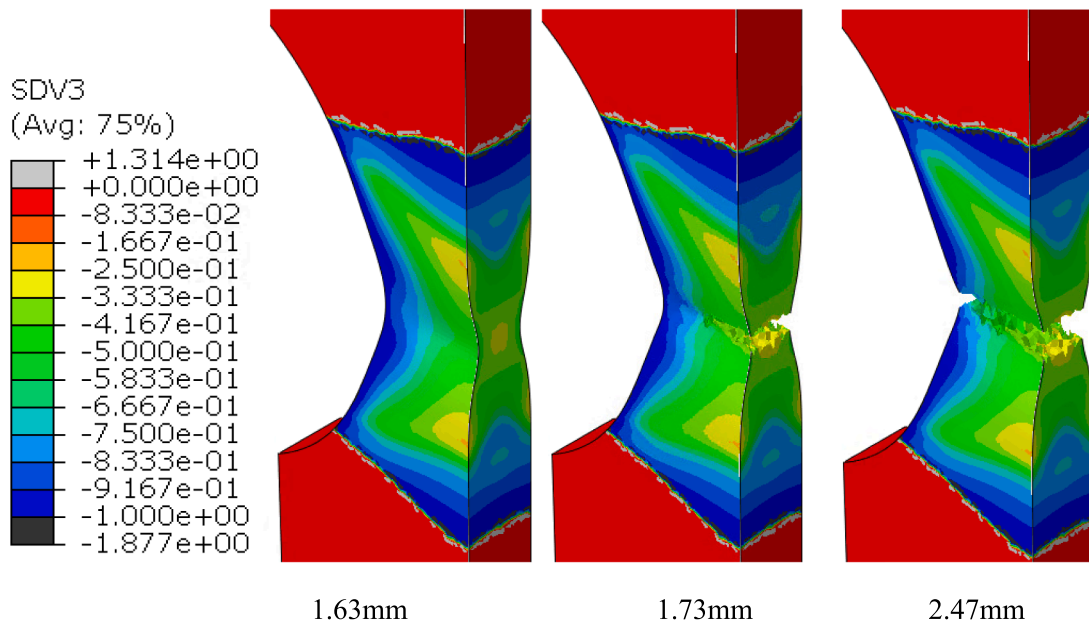
(b) $\bar{L}$

Fig. 15. Crack, stress triaxiality and lode parameter evolution of RN Specimen using maximum MCEPS (Half View).
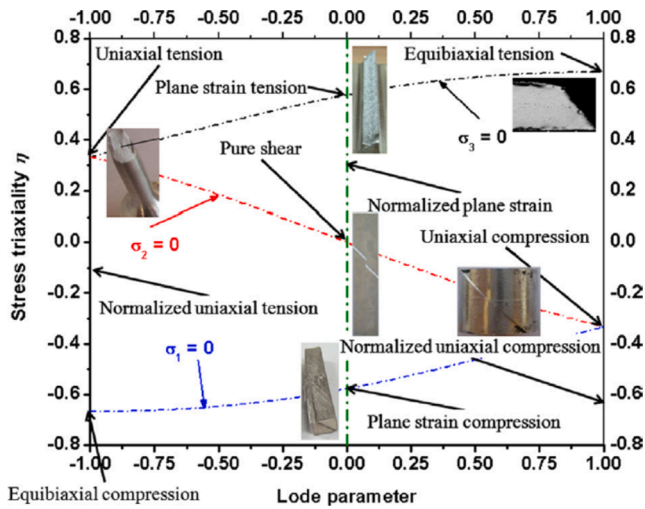
Fig. 16. Stress statues expressed in terms of stress triaxiality and lode parameter [28].

Lode parameter averaged over the loading history of RN specimens are shown in Fig. 15. The crack is initiated in the middle of the specimen and gradually propagated to the round notches of the specimens. The averaged stress triaxiality $\bar{\eta}$ is from 0.6 to 0.67, and the averaged Lode parameter $\bar{L}$ is from -0.33 to -0.25. The stress status of the RN specimen is between uniaxial tensile and plane strain tension, see Fig. 16.
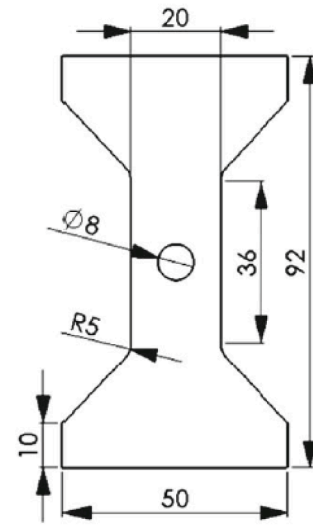
3.2. Specimens with a central hole

The geometry, mesh, and boundary conditions of CN specimens are illustrated in Fig. 17. The force–displacement comparisons of CN specimens between experimental observations and finite element simulation are shown in Fig. 18. The predicted fractures displacement from maximum and homogenized MCEPS and literature [40] is all smaller than test results.

The crack propagation and the evolution of stress triaxiality and the Lode parameter averaged over the loading history of CN specimens are shown in Fig. 19. The crack is initiated in the inner side of the central hole and gradually propagated to the flat surface of the specimens. The averaged stress triaxiality $\bar{\eta}$ is from 0.27 to 0.38, and the averaged Lode parameter $\bar{L}$ is from -0.92 to -1.00. The stress status of the CN specimen is close to uniaxial tensile, see Fig. 16.

3.3. Butterfly specimen

The geometry, mesh, and boundary conditions of butterfly specimens are illustrated in Fig. 20. The force–displacement comparisons of BT and BS specimens between experimental observations and finite element simulation are shown in Fig. 21. The predicted displacement to fracture of BT specimens using the maximum and homogenized MCEPS and literature [40] is all larger than test results while the displacement of the predicted fracture of BS specimens using maximum and homogenized MCEPS and literature [40] is all smaller than test results.

The crack propagation and the evolution of stress triaxiality and the Lode parameter averaged over the loading history of BT and BS specimens are shown in Figs. 22 and 23, respectively. The crack is initiated in the middle of specimens and gradually propagated to the edge for both BT and BS specimens. In terms of BT specimen, the averaged stress triaxiality $\bar{\eta}$ is from 0.87 to 0.95, and the averaged Lode parameter $\bar{L}$ is from -0.10 to 0.00. The stress status of the BT specimen is close to biaxial tension, see Fig. 18. In terms of BS specimen, the averaged stress triaxiality $\bar{\eta}$ and Lode parameter $\bar{L}$ are around 0.0. The stress status of the BS specimen is close to pure shear, see Fig. 18.

(a) Geometry (Unit: mm)[40]
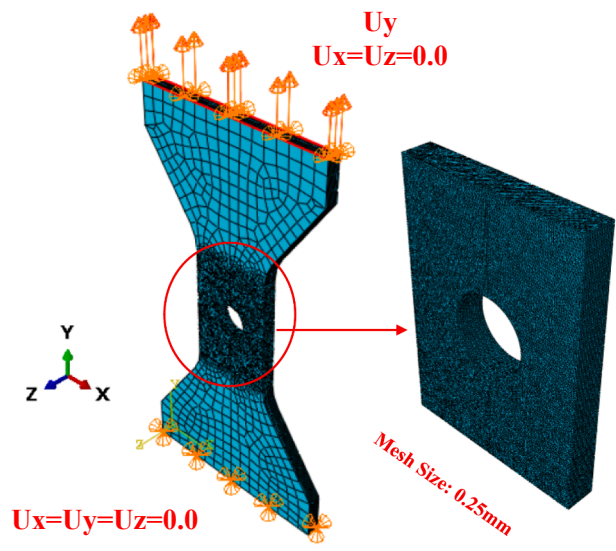
(b) FE model and Boundaries

Fig. 17. Specimens with the central hole (CN) with a thickness of 3.124 mm.
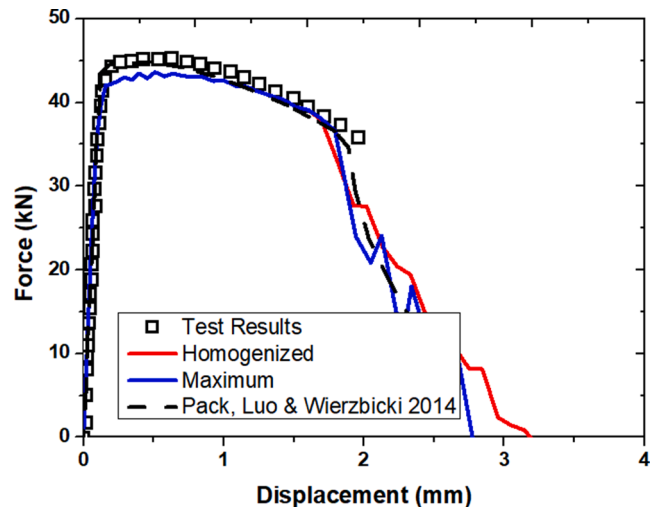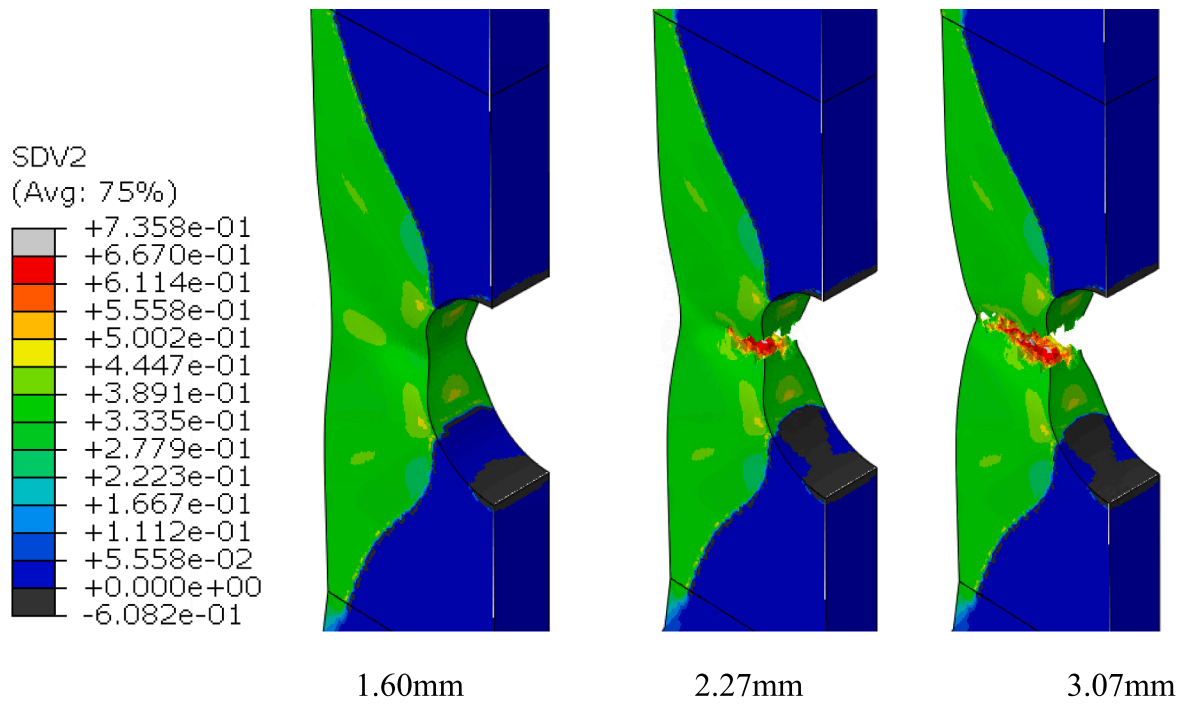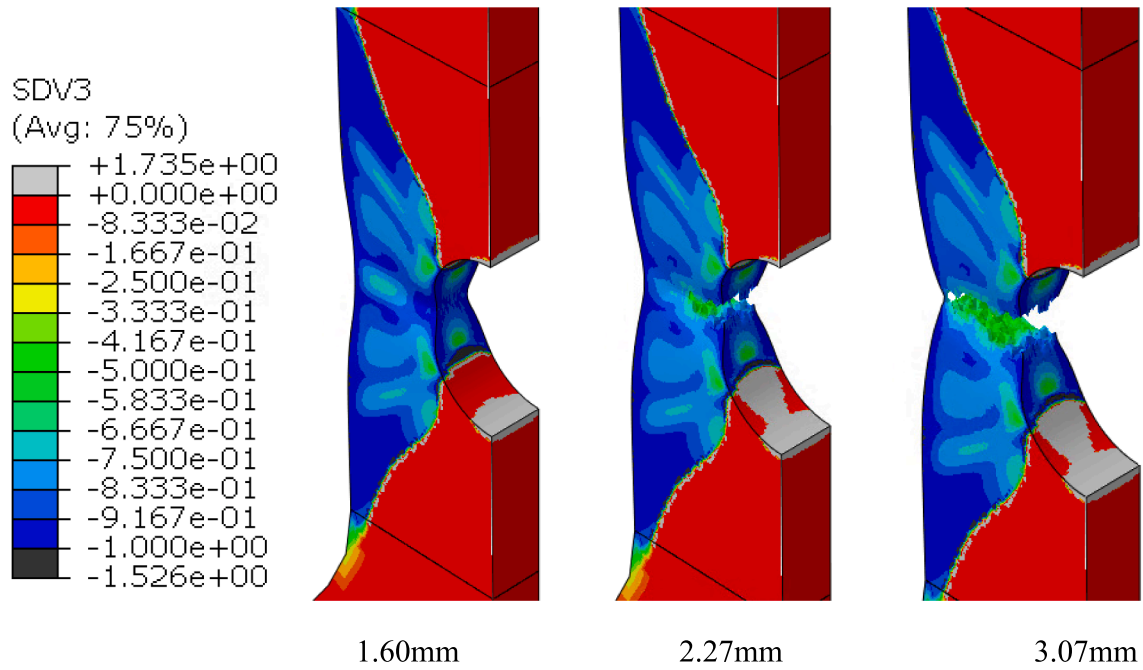

Fig. 18. Comparisons of force-displacement of CN specimen between experimental observations and finite element simulation.
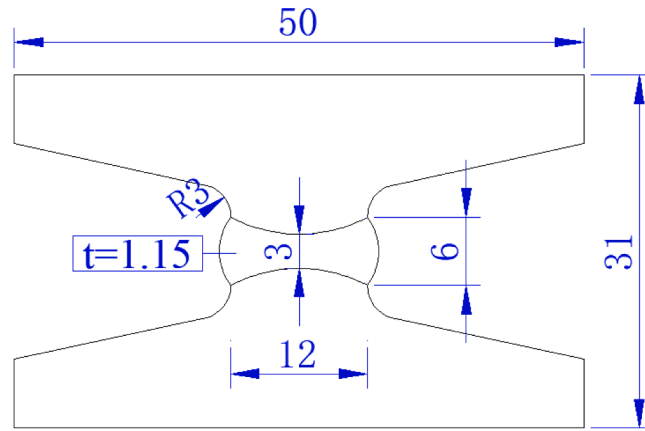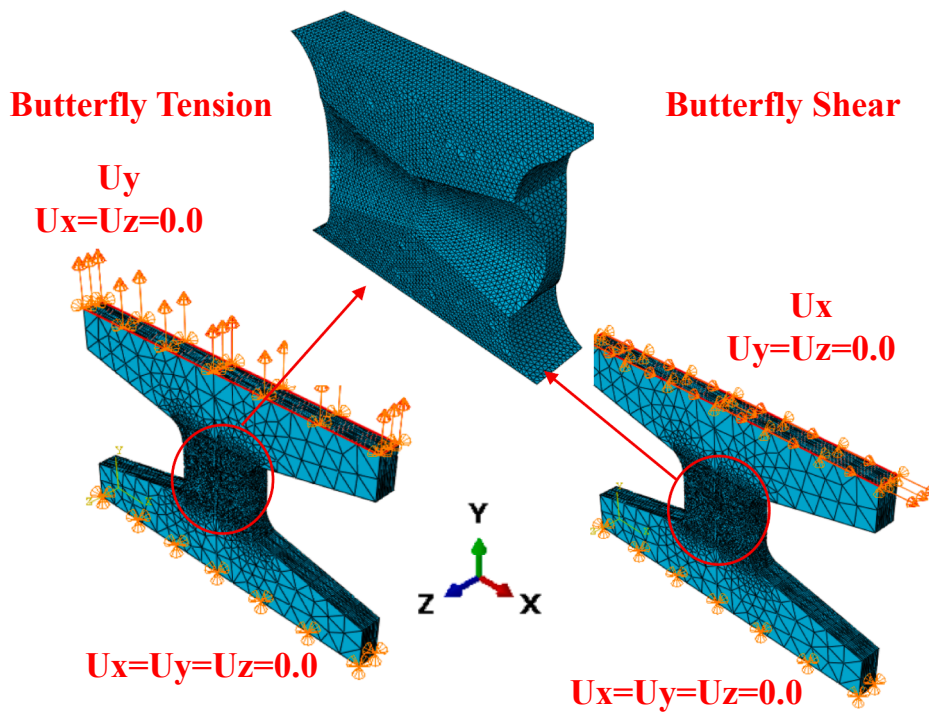
(a) $\overline{}$

(b) $\overline{L}$

Fig. 19. Crack, stress triaxiality and lode parameter evolution of CN Specimen using maximum MCEPS (Half View).
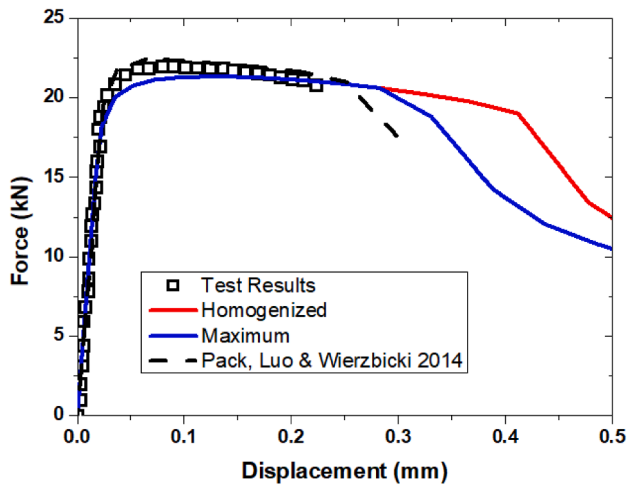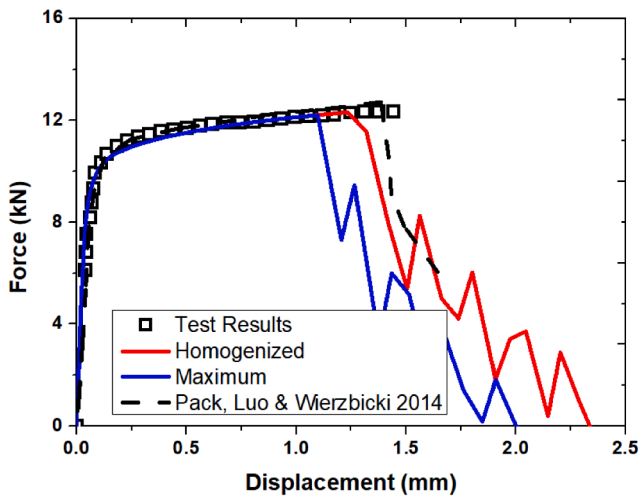
(a) Geometry (Unit: mm) [40]

(b) FE model and Boundaries

Fig. 20. Butterfly specimen with a thickness of 3.124 mm.

(a) Butterfly tensile

(d) Butterfly shear

Fig. 21. Comparisons of force-displacement of butterfly specimens between experimental observations and finite element simulation.

3.4. Discussion of the validation

The displacement to fracture of the butterfly shear(BS) specimen, butterfly tension(BT) specimen, tension specimen with symmetric round notches (RN), tension specimen with a central hole(CN) is presented in Fig. 24. The displacement to fracture (DF) errors χ_i between simulated results and test observation are summarised in Table 4, calculated based on Eq.(18).

The experimental DF of the RN specimen is 5% larger than it predicted based on the maximum MCEPS method, 6% smaller than it predicted based on the homogenized MCEPS method, and 9% larger than it from Pack et al. [40]. The experimental DF of the CT specimen is 8% smaller than it predicted based on the maximum MCEPS method, 12% smaller than it predicted based on the homogenized MCEPS method and 5% smaller than it from Pack et al. [40]. The experimental DF of the BT specimen is 22% smaller than it predicted based on the maximum MCEPS method, and 78% smaller than it predicted based on the homogenized MCEPS method, and 13% smaller than it from Pack et al. [40]. The larger variations between FE simulation and butterfly tests may be from the following reasons: (i) The real boundary of butterfly tests is not accurately simulated; (ii) the common uncoupled damage model on the prediction of ductile fracture with the high-stress triaxiality ($\eta \geqslant \frac{2}{3}$) needs to be further improved. The experimental DF of the BS specimen is 24% larger than it predicted based on the maximum MCEPS method, 13% larger than it predicted based on the maximum MCEPS method, and 4% larger than it from Pack et al. [40].

The average error between FE predicted displacement to fracture and tests results are 15% in terms of the maximum MCEPS method, and 27% in terms of the average MCEPS method, and 8% from Pack et al. [40]. If the displacement at very high-stress triaxiality, $\eta \geqslant \frac{2}{3}$, (BT specimen), is excluded, the average error between FE predicted displacement to fracture and tests results are 12% in terms of the maximum MCEPS method, and 10% in terms of the average MCEPS method, and 6% from Pack et al. [40]. The results showed that the proposed maximum MCEPS method could get comparable results based on the model calibrated from the test series reported in Pack et al. [40], and the homogenized MCEPS method could predict better results than the maximum MCEPS method if the very high-stress triaxiality situation is excluded.

$$\chi_i = \frac{|\delta_{\text{test},i} - \delta_{FE,i}|}{\delta_{\text{test},i}} \quad i = BS, BT, RN, CN \tag{18}$$

0.28mm   0.64mm   1.41mm

(a) $\bar{\eta}$

0.28mm   0.64mm   1.41mm

(b) $\bar{L}$

Fig. 22. Crack, stress triaxiality and lode parameter evolution of FT Specimen using maximum MCEPS (Half View).

SDV2
(Avg: 75%)
+8.837e-01
+3.300e-01
+2.750e-01
+2.200e-01
+1.650e-01
+1.100e-01
+5.500e-02
+2.235e-08
-5.500e-02
-1.100e-01
-1.650e-01
-2.200e-01
-2.750e-01
-3.300e-01
-6.990e-01

-1.09mm   -1.26mm   -2.00mm

(a) $\bar{\eta}$

SDV3
(Avg: 75%)
+1.486e+00
+1.000e+00
+8.333e-01
+6.667e-01
+5.000e-01
+3.333e-01
+1.667e-01
+8.941e-08
-1.667e-01
-3.333e-01
-5.000e-01
-6.667e-01
-8.333e-01
-1.000e+00
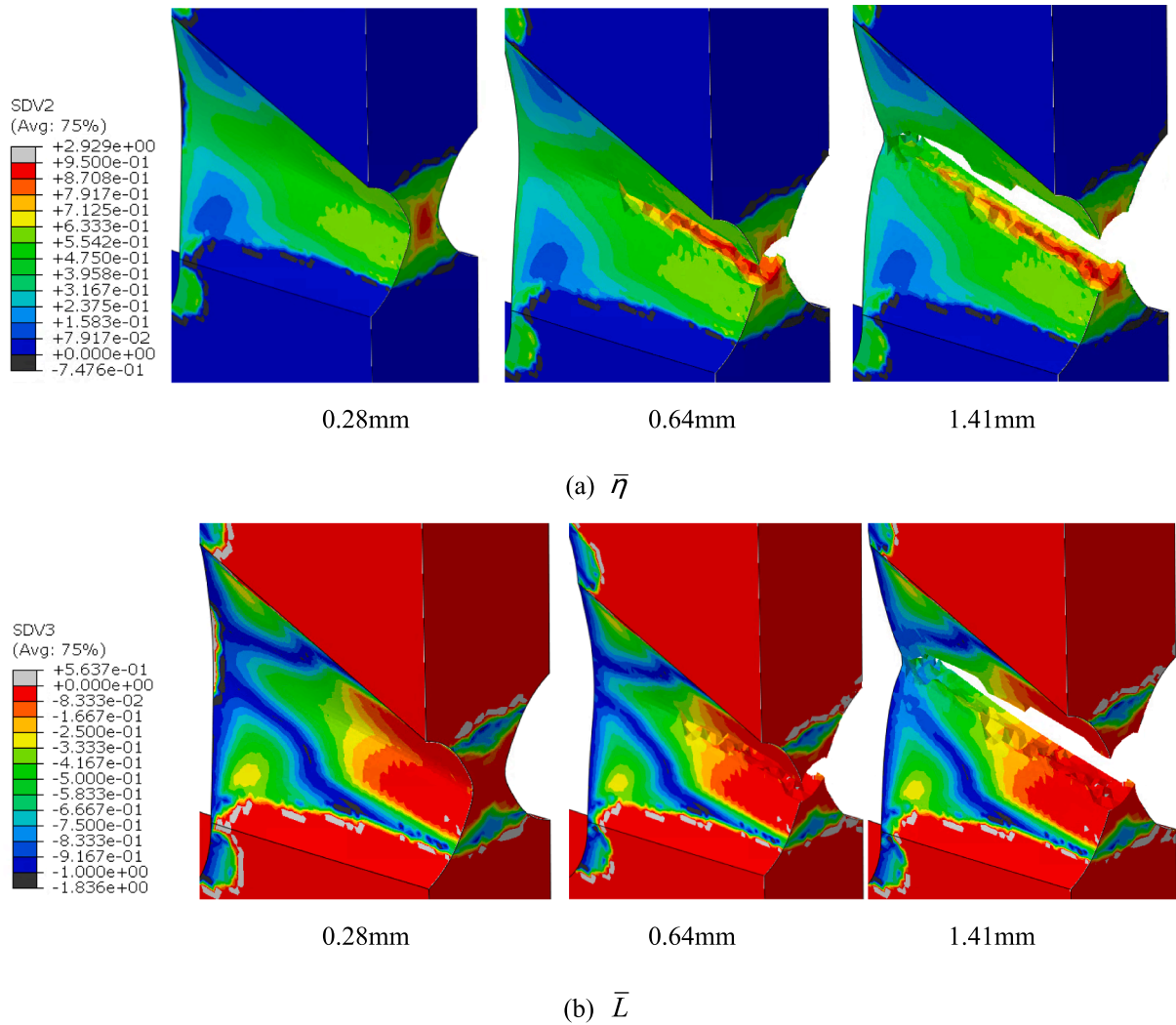-1.358e+00

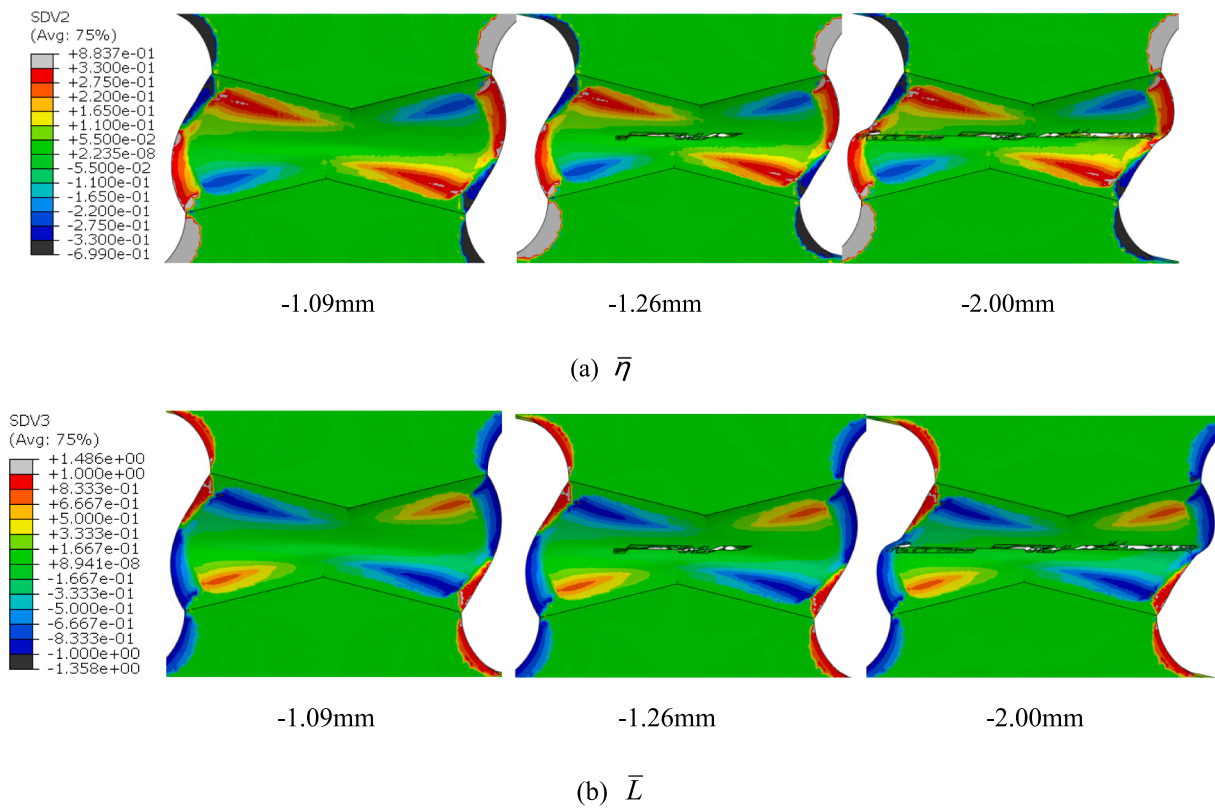-1.09mm   -1.26mm   -2.00mm

(b) $\bar{L}$

Fig. 23. Crack, stress triaxiality and lode parameter evolution of FS Specimen using maximum MCEPS (Half View).
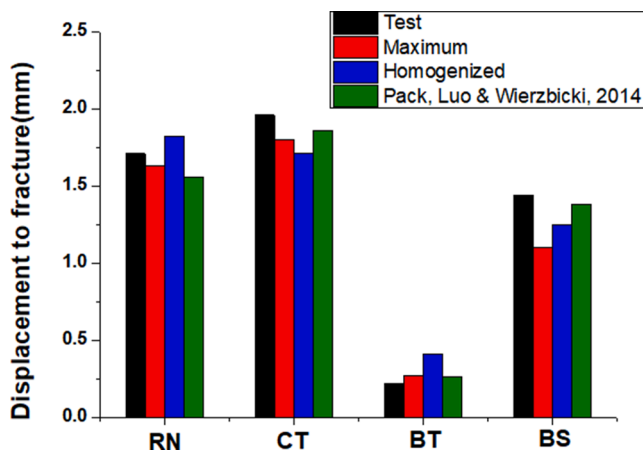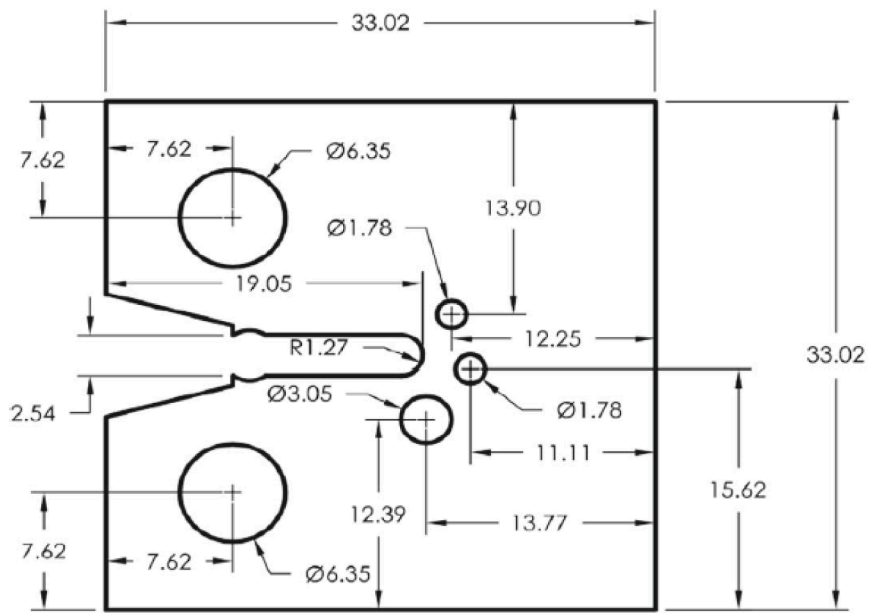

Fig. 24. Evaluation of the predicted displacement to fracture.

Table 4
Error comparisons between FE predicted fracture displacement and test results.

Specimen	Maximum	Homogenized	Pack, Luo & Wierzbicki, 2014
RN	0.05	0.06	0.09
CT	0.08	0.12	0.05
BT	0.22	0.78	0.13
BS	0.24	0.13	0.04
Avergae	0.15	0.27	0.08
Avergae(Exclude BT)	0.12	0.10	0.06

(a) Geometry (Unit: mm) [34]
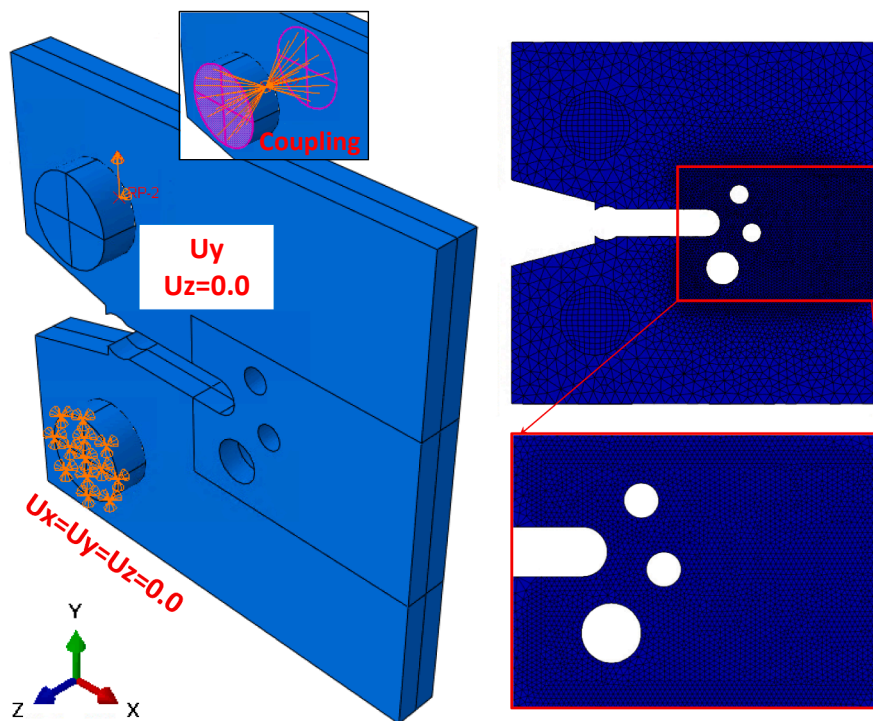
(b) FE model and Boundaries

Fig. 25. Sandia fracture challenge specimens in 2014.
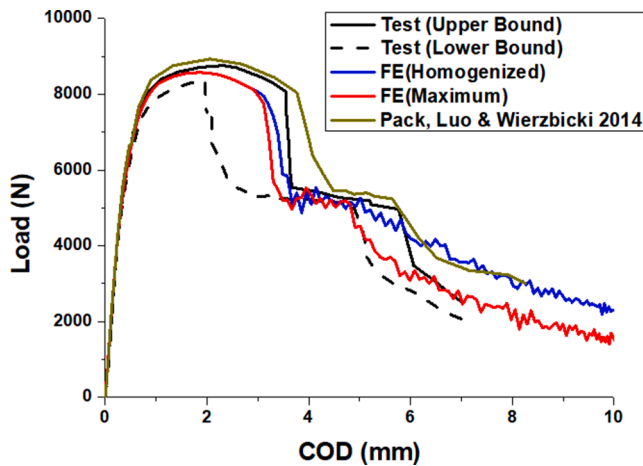
Fig.26. Comparisons of force-displacement of SFC specimen between experimental observations and finite element simulation.

4. Sandia fracture challenge specimens in 2014

The ductile fracture process of the Sandia fracture challenge (SFC) specimen in 2014 [34] is also simulated to validate the identified fracture locus based on the proposed MCEPS failure index. The dimensions, finite element model, and boundary conditions of the SFC specimen are shown in Fig. 25 [34]. The force-crack opening displacement (COD) comparison between FE simulation and experimental results is shown in Fig. 26. A general good agreement is observed for both fracture locus. The fracture locus calibrated using maximum MCEPS as the mesoscale indicator showed a better prediction of the force-COD relationship when the COD is between 5.0 mm and 7.0 mm. Noted that, in terms of the failure mode of the fracture challenge specimen, the experimental force-COD relationship is close to the upper bound. The FE results from the reference[40] presented a slight overestimation of the force when the COD is from 4 mm to 10 mm.

The crack propagation and the evolution of stress triaxiality and the Lode parameter averaged over the loading history of SFC specimens are shown in Fig. 27. When the crack is initiated from the notch to the first hole, the averaged stress triaxiality $\bar{\eta}$ is from 0.22 to 0.55, and the averaged Lode parameter $\bar{L}$ is from -0.67 to -1.00. The stress status of the SFC specimens is between uniaxial tension and plane strain tension, see Fig. 18, when the COD is from 2.68 mm to 3.63 mm. When the crack is propagated from the first hole to the end of the specimen, the averaged

stress triaxiality $\bar{\eta}$ is from 0.33 to 0.44, and the averaged Lode parameter $\bar{L}$ is from -0.67 to 0.0. The stress status of the SFC specimens is also between uniaxial tension and plane strain tension when the COD is larger than 3.82 mm.

5. Conclusion

An attempt is made to identify the parameters of the ductile fracture model conveniently from the uniaxial stress-strain relationship obtained from common coupon specimens. The following conclusions are drawn:

(1) It is relatively difficult to describe the irregular micro-void evolution using the microvoid radius, and also difficult to tackle the micro void coalescence in the mesoscale using void volume fraction. The mesoscale critical equivalent plastic strain (MCEPS) is proposed as the failure index at the unit cell level to calibrate the fracture locus of the uncoupled phenomenological model.

(2) The ductile fractures of butterfly shear(BS), butterfly tension(BT), tension specimen with symmetric round notches(RN), tension specimen with a central hole(CN) are simulated to validate the identified fracture locus. The average error between FE predicted displacement to fracture and tests results are 15% in terms of the maximum MCEPS method, and 27% in terms of the homogenized MCEPS method, and 8% from Pack et al. [40]. If the displacement to fracture of very high-stress triaxiality stress staus (BT specimen) is excluded, the average error between FE predicted displacement to fracture and tests results are 12% in terms of the maximum MCEPS method, and 10% in terms of the homogenized MCEPS method, and 6% from Pack et al. [40]. The proposed maximum MCEPS method could get comparable results based on the model calibrated from the test series reported in Pack et al. [40], and the homogenized MCEPS method could predict better results than the maximum MCEPS method if the very high-stress triaxiality situation is excluded.

(3) The ductile fracture process of the Sandia fracture challenge (SFC) specimen in 2014 [34] is also simulated to validate the identified fracture locus based on the proposed MCEPS failure index. A general good agreement is observed. The fracture locus calibrated using maximum MCEPS as the mesoscale indicator showed a better prediction of the force-COD relationship when the COD is between 5.0 mm and 7.0 mm. The stress status of the SFC specimens is between uniaxial tension and plane strain tension during the crack propagation.

(a) $\bar{\eta}$

(b) $\bar{L}$

Fig. 27. Crack, stress triaxiality and lode parameter evolution of SFC specimen using maximum MCEPS.
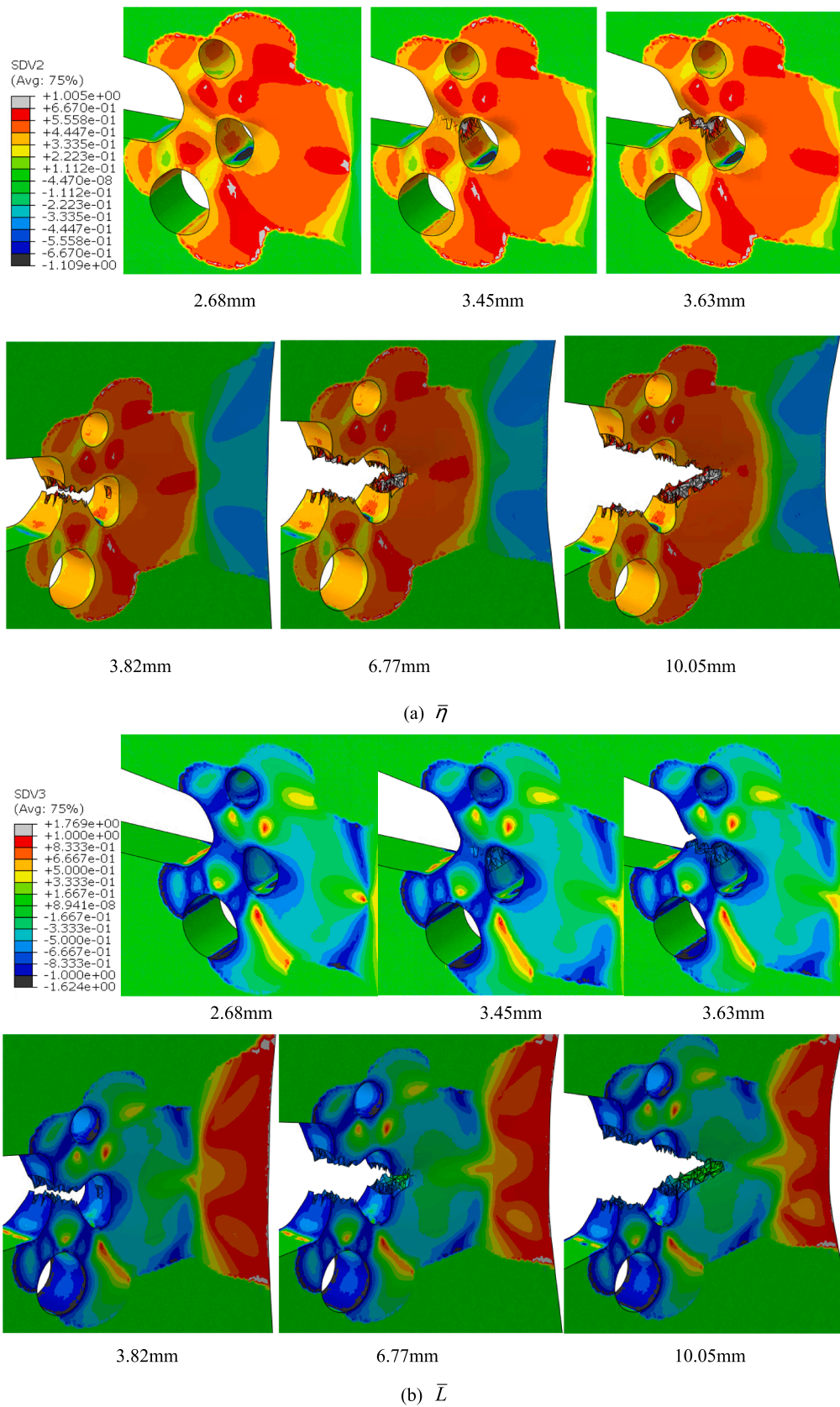
CRediT authorship contribution statement

Haohui Xin: . **José A.F.O. Correia:** Validation. **Milan Veljkovic:** Validation, Supervision. **Filippo Berto:** Validation, Writing - review & editing.

Declaration of Competing Interest

The authors declare that they have no known competing financial interests or personal relationships that could have appeared to influence the work reported in this paper.

Acknowledgments

References

[1] M. Veljkovic, B. Johansson, Design of hybrid steel girders, J. Constr. Steel Res. 60 (2004) 535–547.

[2] H. Xin, M. Veljkovic, Fatigue crack initiation prediction using phantom nodes-based extended finite element method for S355 and S690 steel grades, Eng. Fract. Mech. 214 (2019) 164–176.

[3] H. Xin, J.A.F.O. Correia, M. Veljković, three-dimensional Fatigue Crack Propagation Simulation Using Extended Finite Element Methods for Steel Grades S355 and S690 Considering Mean Stress Effects, Eng. Struct. 227 (2020), 111414.

[4] F. Berto, P. Lazzarin, Recent developments in brittle and quasi-brittle failure assessment of engineering materials by means of local approaches, Mater. Sci. Eng. R Reports 75 (2014) 1–48.

[5] F. Berto, P. Lazzarin, A review of the volume-based strain energy density approach applied to V-notches and welded structures, Theor. Appl. Fract. Mech. 52 (2009) 183–194.

[6] G. Qian, C. Zhou, Y. Hong, Experimental and theoretical investigation of environmental media on very-high-cycle fatigue behavior for a structural steel, Acta Mater. 59 (2011) 1321–1327.

[7] G. Qian, W.-S. Lei, A statistical model of fatigue failure incorporating effects of specimen size and load amplitude on fatigue life, Phil. Mag. 99 (2019) 2089–2125.

[8] G. Qian, W.-S. Lei, M. Niffenegger, V.F. González-Albuixech, On the temperature independence of statistical model parameters for cleavage fracture in ferritic steels, Phil. Mag. 98 (2018) 959–1004.

[9] H. Xin, M. Veljkovic, Residual stress effects on fatigue crack growth rate of mild steel S355 exposed to air and seawater environments, Mater. Des. 108732 (2020).

[10] A.A. Benzerga, J.-B. Leblond, Ductile Fracture by Void Growth to Coalescence, in: Advances in Applied Mechanics, Adv. Appl. Mech., 10 (2010) 169–305.

[11] T.S. Cao, Models for ductile damage and fracture prediction in cold bulk metal forming processes: a review, Int. J. Mater. Form. 10 (2017) 139–171.

[12] J.R. Rice, D.M. Tracey, On the ductile enlargement of voids in triaxial stress fields, J. Mech. Phys. Solids 17 (1969) 201–217.

[13] A.L. Gurson, Continuum theory of ductile rupture by void nucleation and growth: Part I—Yield criteria and flow rules for porous ductile media, 99 (1977) 2–15.

[14] A. Weck, D.S. Wilkinson, Experimental investigation of void coalescence in metallic sheets containing laser drilled holes, Acta Mater. 56 (2008) 1774–1784.

[15] F.A. McClintock, A criterion for ductile fracture by the growth of holes (1968).

[16] V. Tvergaard, Influence of voids on shear band instabilities under plane strain conditions, Int. J. Fract. 17 (1981) 389–407.

[17] V. Tvergaard, A. Needleman, Analysis of the cup-cone fracture in a round tensile bar, Acta Metall. 32 (1984) 157–169.

[18] A.A. Benzerga, J. Besson, Plastic potentials for anisotropic porous solids, Eur. J. Mech. 20 (2001) 397–434.

[19] K. Nahshon, J.W. Hutchinson, Modification of the Gurson model for shear failure, Eur. J. Mech. A. Solids 27 (2008) 1.

[20] L. Xue, Constitutive modeling of void shearing effect in ductile fracture of porous materials, Eng. Fract. Mech. 75 (2008) 3343–3366.

[21] D. Mohr, S.J. Marcadet, Micromechanically-motivated phenomenological Hosford-Coulomb model for predicting ductile fracture initiation at low stress triaxialities, Int. J. Solids Struct. 67 (2015) 40–55.

[22] Y. Bai, T. Wierzbicki, A new model of metal plasticity and fracture with pressure and Lode dependence, Int. J. Plast. 24 (2008) 1071–1096.

[23] Y. Bao, T. Wierzbicki, On fracture locus in the equivalent strain and stress triaxiality space, Int. J. Mech. Sci. 46 (2004) 81–98.

[24] G.R. Johnson, W.H. Cook, A constitutive model and data for metals subjected to large strains, high strain rates and high temperatures, Proc. 7th Int. Symp. Ballist., vol. 21, The Netherlands; 1983, pP. 541–547.

[25] Y. Bai, T. Wierzbicki, Application of extended Mohr-Coulomb criterion to ductile fracture, Int. J. Fract. 161 (2010) 1.

[26] C.C. Roth, D. Mohr, Effect of strain rate on ductile fracture initiation in advanced high strength steel sheets: Experiments and modeling, Int. J. Plast. 56 (2014) 19–44.

[27] S.J. Marcadet, D. Mohr, Effect of compression–tension loading reversal on the strain to fracture of dual phase steel sheets, Int. J. Plast. 72 (2015) 21–43.

[28] M. Lou, J.W. Yoon, H. Huh, Modeling of shear ductile fracture considering a changeable cut-off value for stress triaxiality, Int. J. Plast. 54 (2014) 56–80.

[29] Y. Lou, H. Huh, S. Lim, K. Pack, New ductile fracture criterion for prediction of fracture forming limit diagrams of sheet metals, Int. J. Solids Struct. 49 (2012) 3605–3615.

[30] H. Xin, A. Mosallam, Y. Liu, M. Veljkovic, J. He, Mechanical characterization of a unidirectional pultruded composite lamina using micromechanics and numerical homogenization, Constr. Build. Mater. 216 (2019) 101–118.

[31] H. Xin, M. Veljkovic, Effects of residual stresses on fatigue crack initiation of butt-welded plates made of high strength steel. seventh Int Conf. Struct. Eng. mechancis Comput., Cape Town, 2019.

[32] H. Xin, W. Sun, J. Fish, A surrogate modeling approach for additive-manufactured materials, Int. J. Multiscale Comput. Eng. 15 (2017) 525–543, https://doi.org/10.1615/IntJMultCompEng.2017024632.

[33] M. Achouri, G. Germain, P. Dal Santo, D. Saidane, Experimental characterization and numerical modeling of micromechanical damage under different stress states, Mater. Des. 50 (2013) 207–222.

[34] B.L. Boyce, S.L.B. Kramer, H.E. Fang, T.E. Cordova, M.K. Neilsen, K. Dion, et al., The Sandia Fracture Challenge: blind round robin predictions of ductile tearing, Int. J. Fract. 186 (2014) 5–68.

[35] E. Astm, Standard test methods for tension testing of metallic materials, Annu B ASTM Stand ASTM (2001).

[36] H. XIn, M. Veljković, Evaluation of High Strength Steels Fracture Based on Uniaxial Stress-Strain Curves, Eng. Fail. Anal. 120 (2021) 105025.

[37] Y. Ling, Uniaxial true stress-strain after necking, AMP J Technol 5 (1996) 37–48.

[38] J. Fish, Practical Multiscaling, Wiley, 2013.

[39] V. Abaqus, Documentation, Dassault Syst Simulia Corp 2019 (2019) 651.

[40] K. Pack, M. Luo, T. Wierzbicki, Sandia Fracture Challenge: blind prediction and full calibration to enhance fracture predictability, Int. J. Fract. 186 (2014) 155–175.